

Document Version

Final published version

Licence

CC BY-NC

Citation (APA)

Chen, X., Gadde, S., Droste, A., Steeneveld, G.-J., Coenders-Gerrits, M., & Uijlenhoet, R. (2026). Assessing the role of urban blue space in summer outdoor thermal regulation in northwestern Europe: A hectometric Weather Research and Forecasting modelling on idealized urban landscape. *Quarterly Journal of the Royal Meteorological Society*, Article e70128. <https://doi.org/10.1002/qj.70128>

Important note

To cite this publication, please use the final published version (if applicable).
Please check the document version above.

Copyright

In case the licence states "Dutch Copyright Act (Article 25fa)", this publication was made available Green Open Access via the TU Delft Institutional Repository pursuant to Dutch Copyright Act (Article 25fa, the Taverne amendment). This provision does not affect copyright ownership.
Unless copyright is transferred by contract or statute, it remains with the copyright holder.

Sharing and reuse

Other than for strictly personal use, it is not permitted to download, forward or distribute the text or part of it, without the consent of the author(s) and/or copyright holder(s), unless the work is under an open content license such as Creative Commons.

Takedown policy

Please contact us and provide details if you believe this document breaches copyrights.
We will remove access to the work immediately and investigate your claim.

RESEARCH ARTICLE

Assessing the role of urban blue space in summer outdoor thermal regulation in northwestern Europe: A hectometric Weather Research and Forecasting modelling on idealized urban landscape

Xuan Chen¹  | Srinidhi Gadde² | Arjan Droste¹  | Gert-Jan Steeneveld³  |
Miriam Coenders-Gerrits¹ | Remko Uijlenhoet¹

¹Department of Water Management, Faculty of Civil Engineering and Geoscience, Delft University of Technology, Delft, the Netherlands

²Water Resource Department, Faculty ITC, University of Twente, Enschede, the Netherlands

³Meteorology and Air Quality Section, Wageningen University & Research, Wageningen, Netherlands

Correspondence

Xuan Chen, Department of Water Management, Faculty of Civil Engineering and Geoscience, Delft University of Technology, Delft, the Netherlands.
Email: X.Chen-12@tudelft.nl

Funding information

4TU program HERITAGE (HEat Robustness in Relation To AGEing cities), funded by the High Tech for a Sustainable Future (HTSF) program of 4TU, the federation of the four technical universities in the Netherlands. This work used the Dutch national e-infrastructure with the support of the SURF Cooperative, Grant/Award Number: EINF-2023.042

Abstract

Cities in northwestern Europe face increasingly extreme summer heat under climate change, intensifying the need for effective neighbourhood-scale heat mitigation strategies. Using hectometric (100 m) idealized Weather Research and Forecasting (WRF) simulations during three extreme heat events, this study examines how urban blue space configuration, atmospheric forcing, and physical mechanisms regulate air temperature and thermal comfort (wet-bulb globe temperature index) across coastal and inland cities. We assess how surface energy fluxes interact with horizontal advection to propagate cooling beyond waterbodies, while evaluating whether WRF-Lake produces physically realistic outputs for small, shallow urban blue spaces. Our simulations show near-surface horizontal advection as the dominant cooling mechanism, mixing cooler air from blue spaces with warmer urban air. Around midday, this provides approximately $50 \text{ W} \cdot \text{m}^{-2}$ cooling potential, amplified by evaporative cooling enhanced by urban-generated turbulence. Daily mean temperature reductions ranged from -0.1°C to -0.4°C , with peak morning effectiveness reaching -1.0°C in coastal areas. Wind speed emerged as the primary control: moderate winds ($4.7\text{--}5.8 \text{ m} \cdot \text{s}^{-1}$) propagated cooling citywide, extending up to three times the city diameter downwind, whereas light winds ($1.2 \text{ m} \cdot \text{s}^{-1}$) limited cooling locally. Randomly distributed waterbodies created more homogeneous cooling than canal configurations. Thermal comfort analysis revealed a critical temperature–humidity trade-off. Factor analysis ($R^2 = 0.93$) showed air temperature cooling (50.3%) is counteracted by increased relative humidity (42.3%). We identified limitations of WRF-Lake for shallow urban blue spaces. Default roughness lengths underestimate turbulence and fluxes, likely underestimating cooling and causing unrealistic water temperature increases. This underscores the need for improved parametrizations and targeted observations to advance urban hydrometeorological modelling.

KEYWORDS

advection cooling, blue spaces cooling, hectometric-resolution WRF simulation, urban landscape planning, urban thermal environment

This is an open access article under the terms of the [Creative Commons Attribution-NonCommercial](https://creativecommons.org/licenses/by-nc/4.0/) License, which permits use, distribution and reproduction in any medium, provided the original work is properly cited and is not used for commercial purposes.

© 2026 The Author(s). *Quarterly Journal of the Royal Meteorological Society* published by John Wiley & Sons Ltd on behalf of Royal Meteorological Society.

1 | INTRODUCTION

Urban inhabitants are particularly vulnerable to heat stress due to high population densities and the intensifying effects of the urban heat island phenomenon (Gao *et al.*, 2024; Yang *et al.*, 2019). A widely implemented strategy for mitigating urban heat involves the incorporation of water features, collectively known as urban blue spaces (Fricke *et al.*, 2024), and they influence thermal comfort not only by modifying air temperature but also by altering humidity, wind patterns, and net radiation. Yet, the contribution of each meteorological factor and physical mechanism to blue-space-induced changes in thermal comfort remains poorly quantified. In addition, most studies indicate that evaporation from blue spaces enhances latent heat flux while reducing sensible heat flux contributes to lower air temperature (Tominaga *et al.*, 2015; Zhang *et al.*, 2025). Furthermore, the high heat capacity of water creates low surface temperature, thereby contributing to reducing the urban heat island (Hathway & Sharples, 2012; Lin *et al.*, 2020). Aside from lower surface temperatures, the presence of surfaces with temperature difference gives rise to thermal heterogeneity, which can create persistent horizontal advective fluxes (Cuxart *et al.*, 2016). In the absence of high-resolution neighbourhood-scale simulations (hectometric, 100 m), most studies to date have focused only on evaporation and lower surface temperature as the principal mechanisms of thermal regulation at the regional scale (Ampatzidis & Kershaw, 2020) and have overlooked quantifying the contribution of blue-space-induced local horizontal advection as a cooling mechanism. This necessitates the need for high-resolution neighbourhood-scale simulations that resolve blue spaces to understand the role of horizontal advection in regulating neighbourhood temperatures.

Over the past two decades, summer air temperatures have risen faster over northwestern Europe (Rousi *et al.*, 2022) than other temperate oceanic regions (Cfb; Beck *et al.*, 2023), with extreme heat events exceeding 40°C becoming more frequent (García-Herrera *et al.*, 2010; Yiou *et al.*, 2020). Despite increasing thermal stress on public health and urban systems (Matthews *et al.*, 2025; Tripathy & Mishra, 2023), studies on urban blue space cooling in northwestern Europe remain limited compared with Asia and Australia (Fricke *et al.*, 2024). Within this region, thermal impacts vary considerably between coastal and inland cities. Theeuwes *et al.* (2013) showed that a lake in an inland city reduces daytime air temperature by over 1.5°C but increases night-time temperature by 1°C, with humidity reducing perceived cooling by up to 60%. In contrast, coastal Rotterdam studies (Jacobs *et al.*, 2020; Steeneveld *et al.*, 2014) found different night-time responses, indicating fundamentally different thermal dynamics between

these settings. Comparisons across coastal and inland environments, however, remain lacking.

Beyond location, spatial configuration significantly shapes thermal effects. Studies based on surface temperature analysis have identified patch size thresholds and connectivity as key factors for surface cooling (Peng *et al.*, 2022; Wu *et al.*, 2021; Yujie *et al.*, 2023). Numerical modelling approaches to study blue-space configuration can be classified into two categories: simulations of real urban landscape that reproduce actual urban environments with specific land use patterns, and simulations of idealized urban landscape that systematically test controlled scenarios under real atmospheric conditions. Based on Weather Research and Forecasting (WRF) simulation of an idealized urban landscape, Theeuwes *et al.* (2013) investigated the cooling effect from different sizes of lakes, showing that a single large lake cools more effectively than multiple smaller lakes of equal area. Though simulations of real urban landscape provide site-specific insights (Ding & Chen, 2024), idealized landscape approaches enable systematic comparison of design alternatives by isolating specific spatial factors. Despite these insights, how interconnected canal networks affect thermal regulation remains poorly understood. Urban canal networks vary widely, ranging from scattered ponds in unplanned developments to the orthogonal grids of Suzhou, China, or the winding radial patterns of Amsterdam, Netherlands. Yet, whether these configurations produce distinct cooling patterns through altered advection or evaporation has not been examined through controlled comparative analysis.

Investigating the effect of blue spaces on thermal regulation at the neighbourhood scale requires appropriate numerical tools. Previous simulations treated waterbodies solely with land-surface models, without activating lake parametrizations, thereby failing to simulate water-temperature dynamics and the associated water-body energy balance (Subin *et al.*, 2012). The WRF-Lake module (Gu *et al.*, 2016; Subin *et al.*, 2012) offers a potential solution for representing these waterbodies. Though recent hectometric-scale (100 m) WRF studies have advanced urban atmospheric modelling (Forster *et al.*, 2024; Koopmans *et al.*, 2023; Ronda *et al.*, 2017), they represented only large waterbodies, such as rivers and major lakes, neglecting the shallow canals and ponds (typically 1–5 m deep) that characterize neighbourhood-scale blue infrastructure (Zhu *et al.*, 2022). However, the WRF-Lake module was primarily developed for large, deep lakes with vertical stratification and thermal dynamics fundamentally different from small and shallow urban features. Small and shallow waterbodies experience rapid diurnal heating and cooling due to limited thermal mass, complete vertical mixing that eliminates stratification, enhanced evaporation from high surface-to-volume ratios,

and modified energy exchanges from lateral boundary effects and building shading. Although the WRF-Lake parametrization has been shown to perform reasonably well over large natural lakes (Guo *et al.*, 2022; Wang *et al.*, 2019; Xu *et al.*, 2016), its applicability to shallow, urban blue spaces remains largely unexplored. In this study, we do not aim to perform a formal validation of the lake model. Instead, we conduct a first-order plausibility assessment to examine whether the simulated surface energy fluxes over idealized urban waterbodies exhibit physically consistent and reasonable behaviour.

To address these knowledge gaps, this study employs hectometric (100 m) grid resolution idealized WRF simulations to investigate urban blue spaces in northwestern Europe during summer. We adopt the idealized land-use set-up (Theeuwes *et al.*, 2013; Yang *et al.*, 2024). Although simulations on real urban landscapes reproduce specific urban environments, simulations on idealized urban landscapes prescribe homogeneous land-use tiles within designated domains, enabling systematic testing of alternative spatial configurations under identical real atmospheric forcing. This approach allows us to isolate and compare the effects of blue-space design while maintaining realistic meteorological boundary conditions. We examine three distinct spatial configurations with a constant 30% water coverage: (a) randomly distributed waterbodies, representing unplanned modern development; (b) orthogonal criss-crossing canals, representing planned grid networks typified by cities like Suzhou; and (3) winding organic canals, representing evolved radial systems, like Amsterdam's structure. These configurations are simulated for both coastal and inland cities across three recent summer periods with contrasting synoptic conditions. Using this approach, we address the following research questions (Section 3 and 4):

1. How do different spatially configured urban blue spaces affect thermal comfort across different convective events and city types (coastal vs. inland)?
2. What are the relative contributions of the surface energy fluxes, and is local horizontal advection an important contributor to the observed cooling?
3. To what extent does the WRF-Lake parametrization exhibit physically consistent behaviour when applied to small and shallow urban blue spaces?

Answering these questions advances understanding of urban blue-space thermal regulation in northwestern Europe through three contributions. First, quantifying air temperature responses across different contexts reveals how temporal dynamics, spatial arrangement, and atmospheric conditions modulate cooling effectiveness. Second, decomposing physical mechanisms

clarifies the roles of surface energy fluxes and advection in regulating air temperature and identifies individual meteorological factors' contributions to thermal comfort. Third, discussing the WRF-Lake parametrization identifies its limitations for shallow urban features and guides future neighbourhood-scale modelling improvements. These insights benefit both urban climate adaptation strategies and hectometric-scale simulation development.

2 | METHODOLOGY

2.1 | Study location and period

The numerical experiments conducted in this study employ idealized land surface simulations, following the methodologies of Yang *et al.* (2024) and Theeuwes *et al.* (2013). This experimental design facilitates a systematic comparison of cases characterized by varying spatial configurations of urban blue spaces. Consequently, the specific site selection is not primarily influenced by land-use characteristics, but rather by the distance to the coastline and the requirement that the selected sites be meteorologically independent while situated within the same climatic region. Two urbanized locations in northwestern Europe were selected for this purpose (Figure 1). The coastal city corresponds to the location of Den Haag, Netherlands (latitude 52.16°N, longitude 4.35°E), whereas the inland city corresponds to Brussels, Belgium (latitude 50.82°N, longitude 4.37°E), located approximately 90 km from the shoreline. The proximity of these sites ensures that they are subject to similar large-scale atmospheric conditions, and their spatial separation allows for independent local-scale dynamics.

Specific weather events were selected to represent distinct synoptic and mesoscale atmospheric conditions that are known to influence surface thermal dynamics in different ways. First of all, hot days were chosen to evaluate the thermal impact of persistent high-temperature conditions, which are critical for assessing heat stress and the potential cooling effects of blue spaces. We follow the definition of summer hot days with the daily maximum 2-m air temperature exceeding or equal to 30°C (European Environment Agency, 2025) based on European Centre for Medium-Range Weather Forecasts Reanalysis v5 (ERA5) data (2005–2024 Hersbach *et al.*, 2020). In total, 17 days are defined as hot days at both locations.

We then selected three hot events under different weather patterns, and Supporting Information Figure S1 shows the diurnal variation of spatially averaged 2-m air temperature over land and rainfall rate, along with geopotential height field, gradient, and wind field at 500 hPa

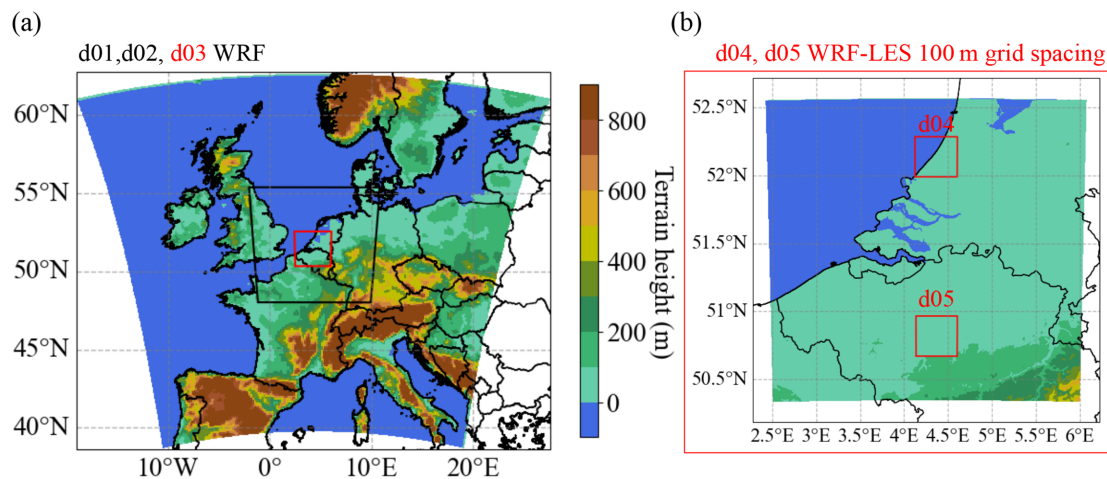


FIGURE 1 Illustration of the Weather Research and Forecasting (WRF) simulation (a) domains 1 to 3 and (b) two nested domains for coastal and inland cities. Domains 4 and 5 are the same size at the two locations with the same parent domain. LES: large-eddy simulation. [Colour figure can be viewed at [wileyonlinelibrary.com](https://onlinelibrary.wiley.com)]

with the wind field at 1200 UTC on the three days we selected:

- Event 1. Hot day without rainfall in both locations (July 24, 2019).
- Event 2. Hot day in both locations, afternoon convective rainfall in the inland city (August 9, 2020).
- Event 3. Hot day in both locations, but heavy rainfall followed 1 day after (August 7, 2018).

Event 1 (no precipitation) represents persistent high temperatures under clear-sky conditions, with daily maximum 2-m air temperatures of 31.6°C (coastal) and 35.0°C (inland). Event 2 captures short-duration convective rainfall effects, defined as afternoon rainfall days based on ERA5 data, with maximum temperatures of 30.4°C (coastal) and 33.8°C (inland). Event 3 examines transitional weather patterns where heavy rainfall follows prolonged heat. Maximum temperatures reached 31.8°C (coastal) and 34.6°C (inland) before rainfall began on August 7, followed by temperature drops and extreme rainfall on August 9 (20.1 and 19.2 mm · day⁻¹). Heavy rainfall days are defined as exceeding the 99th percentile threshold from the past 20 years (18.1 mm · day⁻¹ and 19.0 mm · day⁻¹ for coastal and inland locations respectively; Pendergrass, 2018). All values represent spatial means over ERA5 grid cells (0.25° × 0.25°).

2.2 | WRF idealized simulation set-up

The numerical simulations are performed using the WRF model version 4.6.1 (Skamarock *et al.*, 2019). The basic WRF configuration refers to the set-up of Ronda *et al.* (2017) and Koopmans *et al.* (2023). Two sets of

four one-way nested domains were adopted in the simulation. Figure 1a shows the first three outer domains. Figure 1b shows the two innermost domains (d04 and d05) set for the coastal and inland locations. The vertical grid contained 48 full sigma levels from the surface up to 10 hPa. The selected physical parametrization schemes are listed in Table 1. In this study, the turbulence for the innermost domains was partly resolved and partly modelled with the three-dimensional Smagorinsky first-order closure scheme. The single-layer urban canopy model parametrizes the effect of the built-up area, and the one-dimensional WRF-Lake module solves the urban blue space (Kusaka *et al.*, 2001; Obulkasim *et al.*, 2025; Subin *et al.*, 2012).

We examine the impacts of urban blue spaces and their placement through Real Atmosphere, Ideal Land surface simulations, following the methodology of Yang *et al.* (2024) and Theeuwes *et al.* (2013). In this approach, the atmospheric component is initialized with three-dimensional, spatially heterogeneous variables derived from reanalysis data, whereas the land component in the innermost domains is initialized with spatially uniform, idealized conditions. Initial and boundary meteorological conditions are derived from six-hourly ERA5 pressure level data (38 vertical levels).

The model employs five one-way nested domains, two parallel innermost domains at 100 m resolution, each 32.1 km × 32.1 km (Table 1). Only the innermost domains use idealized land-surface settings; all outer domains maintain realistic land use to ensure consistency with ERA5 forcing. This design isolates local land-use effects (< 2% of the total domain area) while preserving realistic synoptic-scale atmospheric conditions through one-way nesting.

TABLE 1 Weather Research and Forecasting simulation configuration schemes.

Horizontal grid size (m)	12,500, 2500, 500, and 100
Vertical resolution at bottom (m)	50
Grid points	200 × 200, 321 × 321, 481 × 481, and 321 × 321
Microphysical scheme	Thompson scheme (Thompson <i>et al.</i> , 2008)
Boundary-layer scheme	Yonsei University scheme (d01–03) (Hong <i>et al.</i> , 2006)
Eddy coefficient option	Horizontal Smagorinsky first-order closure (d01–03) Smagorinsky first-order closure (three-dimensional) (d04, d05)
Long-wave scheme	Rapid radiative transfer model (Mlawer <i>et al.</i> , 1997)
Short-wave scheme	Dudhia scheme (Dudhia, 1989)
Surface-layer scheme	Revised MM5 Monin–Obukhov scheme (Jiménez <i>et al.</i> , 2012)
Land-surface model scheme	Noah land-surface model (Chen & Dudhia, 2001)
Urban land-surface model scheme	Single-layer urban canopy model (Kusaka <i>et al.</i> , 2001)

Two land-use scenarios are examined in the innermost domain: a “no-city” baseline with homogeneous agricultural land, and urban scenarios with varying blue-space configurations. The baseline uses domain-averaged surface characteristics from moderate-resolution imaging spectroradiometer land-use data (Broxton *et al.*, 2014), with flattened terrain and uniform soil properties (silty clay loam, four vertical layers). Urban scenarios combine moderate-resolution imaging spectroradiometer cropland and lake categories (Broxton *et al.*, 2014) with World Urban Database and Access Portal Tools Local Climate Zone classifications (Ching *et al.*, 2018), where built-up areas correspond to LCZ1 (Stewart & Oke, 2012). All blue spaces have uniform 3-m depth (Jacobs *et al.*, 2020). Surface temperatures are initialized using surface-type-specific domain averages from ERA5-based conditions: blue spaces at 293.8 K (domain-averaged water temperature) and land surfaces at domain-averaged land temperature, whereas ocean surfaces retain their realistic spatial distribution. This surface-type-specific averaging maintains thermodynamic consistency by eliminating artificial horizontal temperature gradients within each surface type while preserving realistic temperature differences between types, ensuring thermal effects arise from land–atmosphere interactions rather than heterogeneous initial conditions.

2.3 | Numerical experiments

In total, 15 simulations are conducted for three selected summer events. Each event includes one control simulation (CTL) and four experimental cases (Figure 2), designed to investigate the impact of different configurations of urban blue spaces. The CTL adheres to the “no-city” configuration with homogeneous agricultural land (Figure 2a,b). Urban cases without water (U1W0) feature a built-up area with 8 km radius represented by LCZ1 (Figure 2c,d).

For cases incorporating urban blue spaces, the water surface fraction within the city is maintained at 30%, based on typical water coverage in European cities ranging from 6% in Berlin to 25% in city centres and 35% in Amsterdam as a whole (City of Amsterdam, 2025; Theeuwes *et al.*, 2013). We first examine the general urban and blue-space impacts by comparing CTL, U1W0, and urban cases with 30% randomly distributed water surface (U7W3r; Figure 2e,f). The random distribution represents a baseline scenario where waterbodies are placed opportunistically without systematic spatial planning.

To investigate whether spatial organization of blue spaces influences cooling effectiveness, we design two additional configurations representing contrasting urban water network designs. The criss-crossing canal case (U7W3c; Figure 2g,h) features an orthogonal grid pattern with canals oriented in perpendicular north–south and east–west directions, inspired by the systematic canal layout of Suzhou, China. This configuration represents planned, geometric water networks with regular spacing and consistent channel widths, facilitating uniform water distribution across the urban domain. The winding canal case (U7W3w; Figure 2i,j) features organic, curved waterways arranged in a radial or semi-concentric pattern, inspired by Amsterdam’s historic canal structure. This configuration represents evolved water networks that developed incrementally, with variable channel orientations and connectivity. Both canal configurations maintain identical 30% water surface fraction but differ fundamentally in network topology, channel orientation patterns, and spatial connectivity, allowing us to isolate the effect of blue-space geometry on thermal regulation. The spatial configurations are kept identical for both coastal and inland city scenarios. Each simulation covers 30 hr, comprising a 6-hr spin-up period followed by a 24-hr analysis period.

Urban effects are quantified by comparing U1W0 against CTL, whereas water effects are determined from differences between water-inclusive cases (U7W3r, U7W3c, U7W3w) and U1W0. Kolmogorov–Smirnov tests assess how water surface placement affects thermal impact distributions. The Kolmogorov–Smirnov

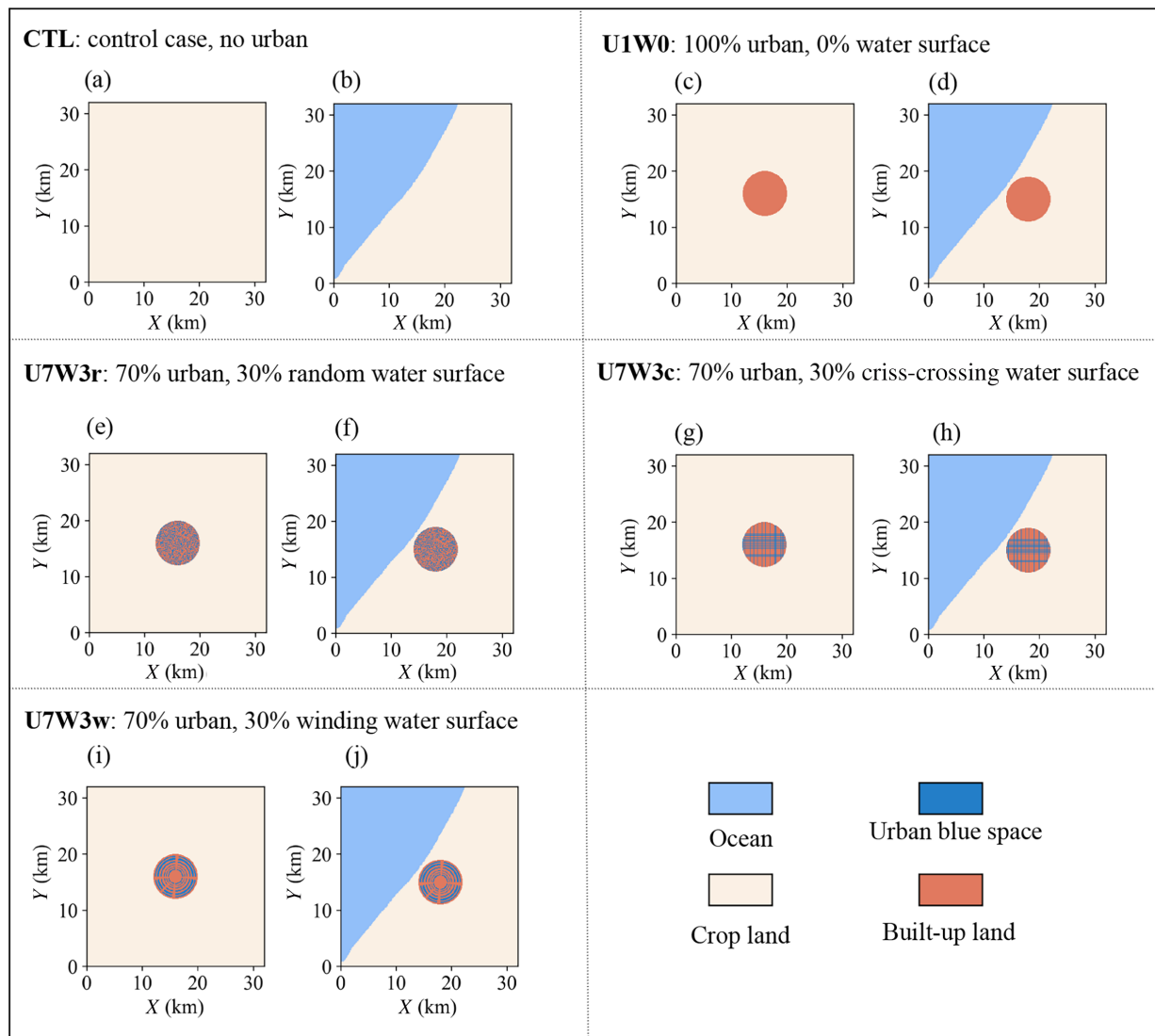


FIGURE 2 Land-use types in the innermost model domains for different simulations over coastal and inland areas: (a, b) control cases (CTL); (c, d) urban cases without water features (U1W0); (e, f) urban cases with randomly distributed water surfaces (U7W3r); (g, h) urban cases with criss-crossing canals (U7W3c); and (i, j) urban cases with winding canals (U7W3w). [Colour figure can be viewed at [wileyonlinelibrary.com](https://onlinelibrary.wiley.com/doi/10.1002/qj.70128)]

statistic quantifies the maximum difference between cumulative distributions of two samples (Lilliefors, 1969; Stephens, 1974), with P values below 0.05 indicating statistically significant differences.

2.4 | Thermal environment analysis

To comprehensively assess outdoor thermal comfort in coastal and inland urban settings, we calculated wet-bulb globe temperature (WBGT) values using explicit physical calculations. Among available WBGT calculation methods, the physical model developed by Liljegren *et al.* (2008) is widely recognized as the standard owing

to its sophisticated treatment of heat and mass transfer principles, careful consideration of sensor geometry, and extensive validation. This approach provides explicit iterative solutions for the natural wet-bulb temperature and incorporates detailed meteorological variables, including temperature components, humidity, and radiation fluxes, rather than relying on empirical approximations.

Following the methodology validated by Kong and Huber (2022), we employed the global-climate-model-specific formulation of the Liljegren *et al.* (2008) algorithm, implemented through the PyWBGT Cython-optimized package. For each 20-min model time step, WBGT variables were systematically extracted from WRF output files. The key input variables included 2-m

air temperature (T_2) and relative humidity (RH_2), surface pressure, 10-m wind velocity components (U_{10} , V_{10}), and cosine of the solar zenith angle. The four radiation components required for the global climate model method were derived directly from WRF diagnostic variables: downward solar radiation, upward solar radiation (computed based on surface albedo), downward long-wave radiation, and upward long-wave radiation (computed from surface skin temperature and emissivity using the Stefan–Boltzmann law).

Factor analysis was conducted to decompose the meteorological drivers of urban water effects on WBGT (Chakraborty *et al.*, 2022). This approach quantifies individual factor contributions to observed thermal differences between urban and water-enhanced environments. The methodology constructs a comprehensive dataset of meteorological variables across both urban-only and water-enhanced scenarios, spanning T_2 , RH_2 , 10-m wind speed (U_{10}), surface net short-wave radiation (S_{Wnet}), for each urban grid cell that remained urban in both scenarios. The water effect ($\Delta X = X_{U7W3_{r/c/w}} - X_{U1W0}$) was calculated for each meteorological variable difference and $\Delta WBGT$ at every time step and spatial domain, ensuring that spatial consistency was maintained in urban grid cells across scenarios. Multiple linear regression models with an intercept were then fitted to the relationship for each event and time step, separately for coastal and inland cities:

$$\Delta WBGT = \beta_0 + \beta_1 \Delta T_2 + \beta_2 \Delta RH_2 + \beta_3 \Delta U_{10} + \beta_4 \Delta S_{Wnet} + \epsilon. \quad (1)$$

The regression coefficients (β_1 – β_4) quantify how much WBGT changes per unit change in each predictor variable. For example, β_1 indicates the WBGT change (in °C) for each 1°C change in air temperature, while holding other factors constant. These sensitivities may differ between coastal and inland settings due to different baseline climates and waterbody characteristics. The intercept β_0 captures baseline differences not explained by the measured variables. ϵ is the residual error term. Each fitted model was subsequently applied to compute factor-specific contributions for each time step and spatial domain by multiplying the observed Delta values by their corresponding regression coefficients. This approach enables us to attribute the relative importance of temperature, humidity, wind, and radiation changes to the overall WBGT differences between urban and water-enhanced environments, providing mechanistic insights into how blue-space interventions modify outdoor thermal comfort through multiple pathways. The R^2 score and root-mean-square error were calculated to check models' robustness. And then each individual factor contribution was calculated and analysed.

2.5 | Surface energy balance

The surface energy balance describes the partitioning of available energy into turbulent and storage heat fluxes. Net radiation for land surfaces is calculated as

$$R_{net} = (1 - \alpha)S_{W\downarrow} + \epsilon(L_{W\downarrow} - \sigma T_{SK}^4), \quad (2)$$

where α is surface albedo, $S_{W\downarrow}$ is downward short-wave radiation, $L_{W\downarrow}$ is downward long-wave radiation, ϵ is surface emissivity, σ is the Stefan–Boltzmann constant ($5.67 \times 10^{-8} \text{ W} \cdot \text{m}^{-2} \cdot \text{K}^{-4}$), and T_{SK} (K) is skin temperature.

For water surfaces in WRF-Lake, short-wave radiation is partitioned based on spectral absorption characteristics. Water transparency causes visible light (60% of solar radiation) to penetrate below the surface, whereas near-infrared radiation (approximately 40%) is absorbed at the surface (Subin *et al.*, 2012). Therefore, net radiation over water is calculated as

$$R_{net} = \beta(1 - \alpha)S_{W\downarrow} + \epsilon(L_{W\downarrow} - \sigma T_{SK}^4) \quad (3)$$

$$Q_{pen} = (1 - \beta)(1 - \alpha)S_{W\downarrow}, \quad (4)$$

where $\beta = 0.4$ represents the fraction of absorbed short-wave radiation available at the water surface for turbulent exchange. The penetrating short-wave radiation, Equation (4), is absorbed in deeper water layers and contributes to subsurface heat storage rather than immediate surface energy partitioning.

The surface energy balance for both land and water surfaces can then be expressed as

$$R_{net} + H_{adv} + LE_{adv} = H + LE - G, \quad (5)$$

where sensible heat flux H , latent heat flux LE , and ground heat flux G represent energy sinks, whereas near-surface horizontal advection of sensible and latent heat, H_{adv} and LE_{adv} , contribute additional energy sources. All terms are in units of watts per metre squared. For water surfaces, G represents heat storage in the surface water layer. It is worth mentioning here that, owing to prominent thermal heterogeneity introduced by the presence of water and land next to each other, the advective heat flux is also included. The calculation of the near-surface advection will be explained in the next section.

2.6 | Heat advection calculation

The presence of distributed water and land surfaces in our WRF simulations gives rise to thermal heterogeneities that have been found to contribute to spatially varying

fluxes (Margairaz *et al.*, 2020). Therefore, it is necessary to quantify the contribution of horizontal advection to the variation of sensible and latent heat fluxes. In this study, horizontal advections ($\text{W} \cdot \text{m}^{-2}$) of the sensible and latent heat are respectively defined as

$$H_{\text{adv}} = \int_0^{Z_{\text{mass}}} \rho C_p \left(\bar{u} \frac{\partial \bar{\theta}}{\partial x} + \bar{v} \frac{\partial \bar{\theta}}{\partial y} \right) dz \quad (6)$$

and

$$LE_{\text{adv}} = \int_0^{Z_{\text{mass}}} \rho \lambda \left(\bar{u} \frac{\partial \bar{q}}{\partial x} + \bar{v} \frac{\partial \bar{q}}{\partial y} \right) dz, \quad (7)$$

in which ρ ($\text{kg} \cdot \text{m}^{-3}$) is the density of air, C_p ($\text{J} \cdot \text{kg}^{-1} \cdot \text{K}^{-1}$) is the specific heat capacity of air at constant pressure, λ ($\text{J} \cdot \text{kg}^{-1}$) is the latent heat of vaporization, $\bar{\theta}$ (K) is the temperature, \bar{q} ($\text{kg} \cdot \text{kg}^{-1}$) is the specific humidity, and \bar{u} and \bar{v} are the horizontal winds in the x and y directions respectively. All the terms are half-hourly averaged. All the advection terms are calculated at the mass points in the WRF Arakawa C-grid. Net advection in a WRF cell is calculated as the integral from the surface to the location of the respective mass point. Here, as we focused on

the near-surface advection, Z_{mass} represents the first model grid level.

For this analysis, we employ WRFlux, an open-source diagnostic tool designed for the WRF model (Göbel *et al.*, 2022). WRFlux facilitates detailed budget evaluations and decomposes resolved advection into mean advective and resolved turbulence components. This capability is particularly valuable for interpreting outputs from large-eddy simulations.

3 | IMPACT OF BLUE SPACE ON URBAN THERMAL ENVIRONMENT

3.1 | Air temperature

Figure 3a–c presents the diurnal profile of the spatial mean 2-m air temperature over the built-up area (LCZ1). The urban heat island effect (U1W0 minus CTL, shown in red-dish bars) exhibits a pronounced diurnal cycle, with peak intensities during night-time and reduced values during daytime. The daily mean urban effect values are 2.0°C, 0.9°C, and 1.6°C for the coastal city, and 1.9°C, 1.5°C,

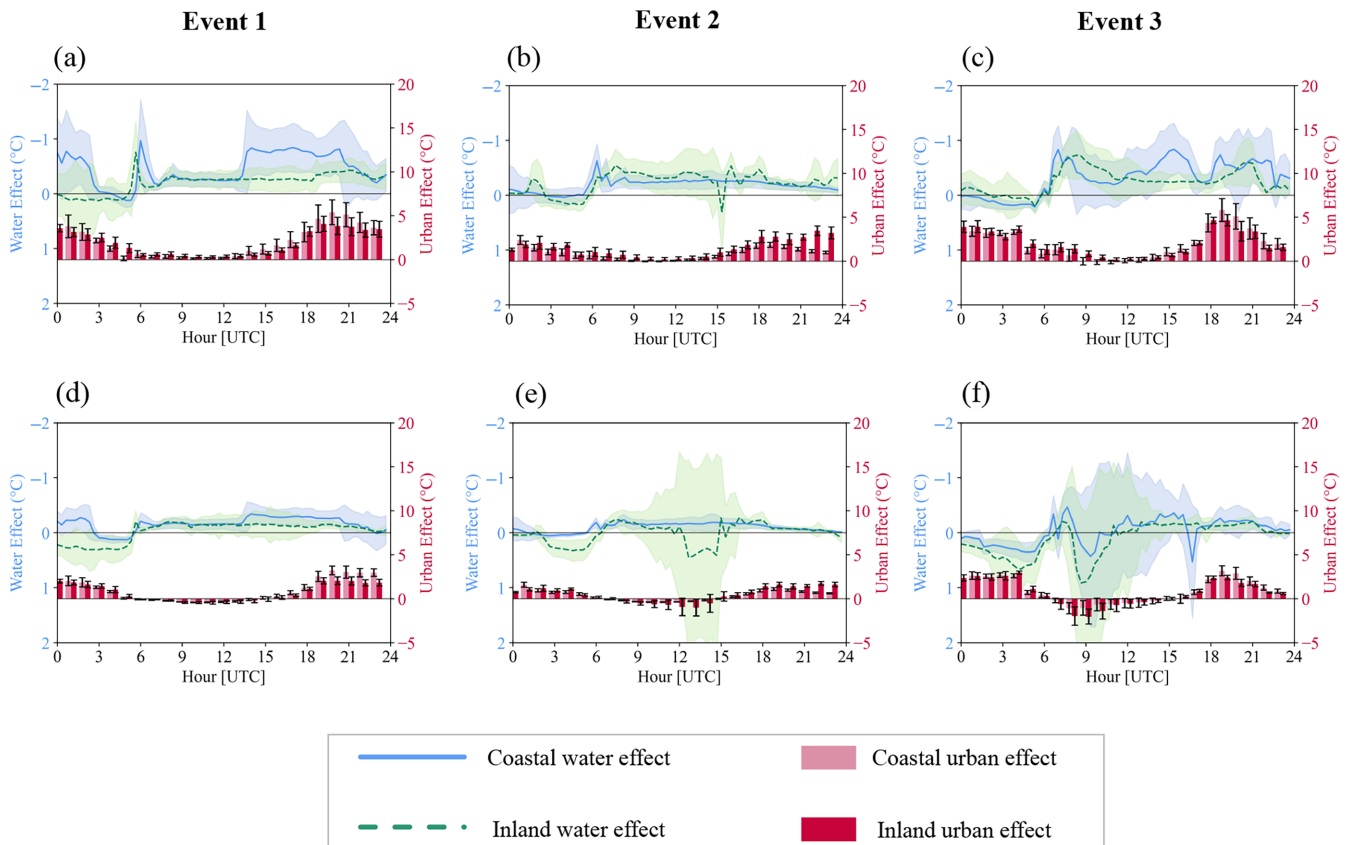


FIGURE 3 (a)–(c) Temporal evolution of the water effect (U7W3 – U1W0) and urban effect (U1W0 – Control) in terms of 2-m air temperature during events 1 to 3. (d)–(f) The corresponding evolution of the effects in terms of wet-bulb globe temperature. [Colour figure can be viewed at [wileyonlinelibrary.com](https://onlinelibrary.wiley.com/doi/10.1002/qj.70128)]

and 1.7°C for the inland city across events 1, 2, and 3 respectively.

The water effect (U7W3 minus U1W0, shown in blue and green lines) demonstrates distinct temporal patterns. Daily mean cooling effects are -0.43°C , -0.22°C , and -0.22°C in the coastal city, and -0.24°C , -0.23°C , and -0.1°C in the inland city for the three events. Blue spaces induce cooling during most of the day and early evening. The peak cooling effect occurs between 0600 and 0800 UTC (morning period) in both cities, reaching a maximum of -1.0°C in terms of T_2 in the coastal area. Note that, in our focus area (UTC + 2 hr), summer sunrise occurs at 0300–0400 UTC and sunset at 1900–2000 UTC. Though the cooling magnitude is generally comparable between coastal and inland cities during most hours, the coastal city exhibits notably enhanced cooling during specific periods, particularly during sea breeze events that are absent in the inland city.

3.1.1 | Morning period cooling

The morning period represents the most effective cooling from urban blue spaces. Figure 4a,b illustrates the spatial

variation in 2-m air temperature difference between cases with randomly placed water surfaces (U7W3r) and without water surfaces (U1W0). The T_2 directly above water surfaces is substantially lower than over built-up land. In event 1, the average ΔT_2 over water surfaces reaches -3.9°C in the coastal city and -3.2°C in the inland city. Similar patterns are observed in events 2 and 3 (Supporting Information Figures S2 and S3). Comparing across the three events reveals that water surfaces are cooler when near-surface wind speed is higher, likely due to enhanced evaporation and stronger turbulent transport under higher wind speeds.

The cooling impact extends beyond the water surfaces into surrounding built-up areas. Averaged across the three events, ΔT_2 over built-up areas is -0.41°C in the coastal city and -0.28°C in the inland city at 0600–0800 UTC. Consistent negative ΔT_2 values are also observed in areas outside the city, downwind from the main wind direction.

Figure 5a–c further examines the spatial extent of morning cooling by showing cooling intensity as a function of distance from upwind water surfaces. The results reveal that wind speed is a primary control on the downwind propagation of the cooling effect. Under general to moderate breeze wind conditions (events 1 and 2, with

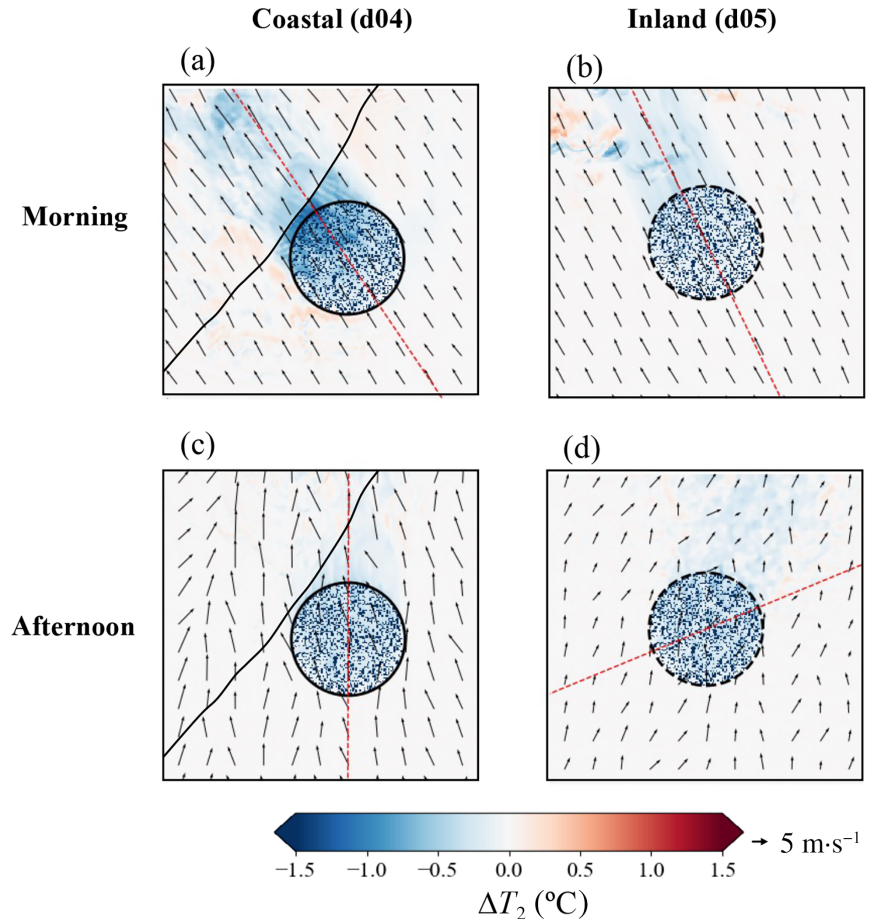


FIGURE 4 Spatial distribution of the mean 2-m air temperature difference ΔT_2 between the U7W3r and U1W0 cases over the central area of the simulation domain in coastal and inland cities during event 1: (a, b) 0600–0800 UTC; (c, d) 1100–1300 UTC. Red dashed lines indicate the dominant surface wind direction. [Colour figure can be viewed at wileyonlinelibrary.com]

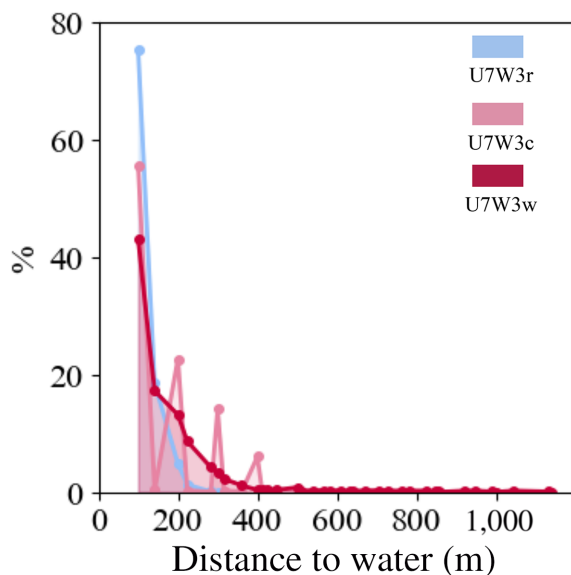


FIGURE 5 Cooling effect of blue-space scenarios on 2-m air temperature. (a)–(c) Change in 2-m air temperature ΔT_2 between blue-space scenarios (U7W3r, U7W3c, U7W3w) and the urban baseline (U1W0) as a function of distance from the upwind water surface during the morning period for events 1–3. (d)–(f) Distribution of 2-m air temperature differences ΔT_2 over built-up grid cells during the afternoon period for the three water placement scenarios in events 1–3. [Colour figure can be viewed at wileyonlinelibrary.com]

average wind speeds of $5.8 \text{ m} \cdot \text{s}^{-1}$ and $4.7 \text{ m} \cdot \text{s}^{-1}$ respectively), negative ΔT_2 values persist over considerable distances, extending 20–25 km downwind from waterbodies. This widespread cooling is facilitated by the stable atmospheric conditions and shallow planetary boundary-layer characteristic of morning hours, which together promote horizontal advection of cool air while suppressing vertical mixing that would otherwise dilute the temperature signal. In contrast, event 3 with light air winds ($1.2 \text{ m} \cdot \text{s}^{-1}$) exhibits a dramatically reduced spatial extent, with the cooling effect confined to approximately 3 km. Under light air wind conditions, the advective transport is insufficient to overcome local mixing processes, limiting the cooling influence to areas immediately adjacent to water surfaces. This contrast underscores the critical role of wind-driven advection in extending the thermal footprint of urban waterbodies during morning hours.

3.1.2 | Afternoon period cooling

Figure 4c,d shows the spatial variation in ΔT_2 during the midday period. The cooling effect over water surfaces intensifies substantially compared with the morning period. The mean ΔT_2 over water surfaces reaches -6.6°C in the coastal city and -5.6°C in the inland city, which are

much larger absolute values than in the morning. Similar to the morning period, the cooling effect above water surfaces is more pronounced under higher wind speeds, and the coastal city exhibits larger cooling intensity compared with the inland city.

However, the cooling effect in built-up areas does not increase proportionally during midday despite the stronger cooling over water surfaces. On average, ΔT_2 over built-up areas in the midday period is -0.3°C in both the coastal and inland cities, similar to or even slightly lower than the morning values. One possible explanation is that deeper planetary boundary layers have a smaller effect on ΔT_2 at the ground due to dilution over a deep planetary boundary layer. Vertical cross-sections along the dominant wind direction (Supporting Information Figures S4 and S5) confirm this interpretation: negative ΔT_2 values are concentrated in the lowest 300 m of the boundary layer shortly after sunrise but can reach up to 1 km in the middle of the day.

In contrast to the morning period, the cooling effect spreading beyond the city is less noticeable in the afternoon, even under high wind speed conditions. This difference may relate to the development of the turbulent atmospheric boundary layer, which starts after sunrise and allows relatively cold air from water surfaces to enter built-up areas, leading to intense cooling during morning hours. Later in the day, the deeper atmospheric boundary layer distributes the cooling over a relatively deep layer, thus weakening the actual surface cooling compared with morning conditions.

Figure 5d–f examines how blue-space spatial configuration affects the distribution of ΔT_2 over built-up grid cells during this period, comparing three water placement scenarios (U7W3r, U7W3c, U7W3w). The distributions in events 1 and 2 show more concentrated patterns, indicating smaller variations in ΔT_2 . This occurs because strong winds spread cooling air more evenly, creating a more homogeneous cooling effect. Conversely, when surface wind speeds are low in event 3 (Figure 5f), ΔT_2 variations are larger.

When comparing different spatial configurations of blue spaces, randomly distributed blue spaces (U7W3r) tend to follow a normal distribution with a single peak, whereas canal cases (U7W3c and U7W3w) exhibit multi-peak distribution characteristics. This difference is more pronounced under strong wind conditions. The distribution differences are significant ($P < 0.05$) based on the Kolmogorov–Smirnov test. The significant difference in ΔT_2 distribution may relate to the distance to blue spaces resulting from different spatial configurations. The reachability of blue spaces for surrounding built-up areas is greater and shows smaller variations in the randomly distributed case (U7W3r) than with the canal cases.

Additionally, canal cases display a wider range of ΔT_2 values. The larger maximum cooling effect in canal cases may be due to the larger contiguous water surface area, whereas the smaller cooling effect (or larger warming effect) may be attributed to reduced reachability.

3.1.3 | Coastal and inland comparison

Though the cooling magnitude from blue spaces is generally comparable between coastal and inland cities during most hours, specific meteorological events reveal important differences in how blue spaces interact with local circulation patterns.

During event 1, the coastal city experiences a pronounced enhancement in cooling effect beginning at 1300 UTC (Figure 3a). This enhanced cooling is attributed to sea breeze circulation, which is present in the coastal city but absent in the inland city. At 1300 UTC, the increase in cooling effect from blue spaces coincides with a strong sea breeze reaching the city edge. The sea breeze intensifies evaporative cooling from water surfaces and advects cooler air deeper into the built-up area. The westerly wind continues to advance, completely shifting the flow from south-to-north to west-to-east by 1500 UTC. This strong westerly wind persists until 2100 UTC, maximizing both evaporative cooling from blue spaces and the transport of cool air into the city, until the cooling effect begins to weaken. In contrast, the inland city shows steady but non-enhanced cooling from its blue spaces throughout the day, lacking sea breeze amplification.

Event 2 reveals a different pattern through complex interactions between blue spaces and urban-induced convection in the inland city (Figure 3b). At 1500 UTC, the inland city experiences a sudden drop in the cooling effect, with the water effect showing positive values (indicating higher T_2 in areas with blue spaces). This phenomenon coincides with convective rainfall over the inland city and may be linked to urban-induced convective precipitation (Yang *et al.*, 2024; Zhang *et al.*, 2022).

Analysis of simulated precipitation across scenarios at the time of peak convective activity (1500 UTC) reveals distinct differences. The urban scenario (U1W0) produces the highest precipitation intensity ($0.94 \text{ mm} \cdot \text{hr}^{-1}$) and total event accumulation (1.0 mm), whereas the control scenario shows the lowest values (peak: $0.096 \text{ mm} \cdot \text{hr}^{-1}$; total: 0.18 mm). The water scenario (U7W3r) exhibits intermediate precipitation levels, with a peak intensity of $0.28 \text{ mm} \cdot \text{hr}^{-1}$ and total accumulation of 0.36 mm, approximately double that of the control but only about one-third of the urban case. These differences support the hypothesis that heated urban surfaces induce more intense convection, resulting in heavier rainfall, especially under

humid atmospheric conditions (Zhu *et al.*, 2017). In contrast, areas with blue spaces, which have lower surface and near-surface temperatures, experience reduced convective rainfall compared with the fully urbanized case (Wang, 2009). The land surface in the U7W3r case is cooler with less rainfall than in the U1W0 case, though still warmer and wetter than the control due to partial urbanization. Given the complexity and sensitivity of the precipitation process, current simulations and set-ups do not allow for definitive conclusions about the role of blue spaces in convection processes (Forster *et al.*, 2024). Ensemble simulations are needed to explore how blue spaces impact moist convection due to the urban heat island.

3.2 | Thermal comfort

Based on the analysis on water effect in WBGT temporal variations, urban waterbodies demonstrate distinct diurnal and event-specific cooling patterns that vary across heat-wave events and spatial domains (Figure 3d–f). The July 2019 heat wave exhibited the consistent cooling effects, with 100% of cases showing net cooling, characterized by peak afternoon cooling at 1500 UTC (-0.31°C) in coastal areas and morning cooling at 0800 UTC (-0.18°C) inland. The warming effect in WBGT over the inland city is shown from 1300 to 1500 UTC in event 2, which is before and during the convective precipitation. In event 3, extreme morning warming peaks reach 0.73°C in inland areas. The diurnal ranges varied substantially, indicating strong temporal variability in waterbody effectiveness across different meteorological conditions and geolocations.

The WBGT factor analysis employed a four-factor delta-based multi-linear regression approach, constructing 432 individual linear models (3 events \times 2 domains \times 72 time steps) with domain-specific and time-step-specific coefficients to capture both spatial and temporal variations in waterbody effects. These models demonstrated excellent predictive skill with a mean R^2 of 0.93, achieving robust performance, with coastal domains ($R^2 = 0.94$) slightly outperforming inland domains ($R^2 = 0.92$), and a mean root-mean-square error of 0.09°C across more than 10,000 sample points per model. The coefficients over the 432 models reveal that air temperature cooling serves as the primary mechanism (50.3% of total contribution), whereas relative humidity warming constitutes the competing secondary mechanism (42.3% contribution).

Figure 6 reveals distinct temporal patterns in waterbody effects on WBGT across different heat events and domains, demonstrating a characteristic diurnal cycle driven by the fundamental temperature–humidity

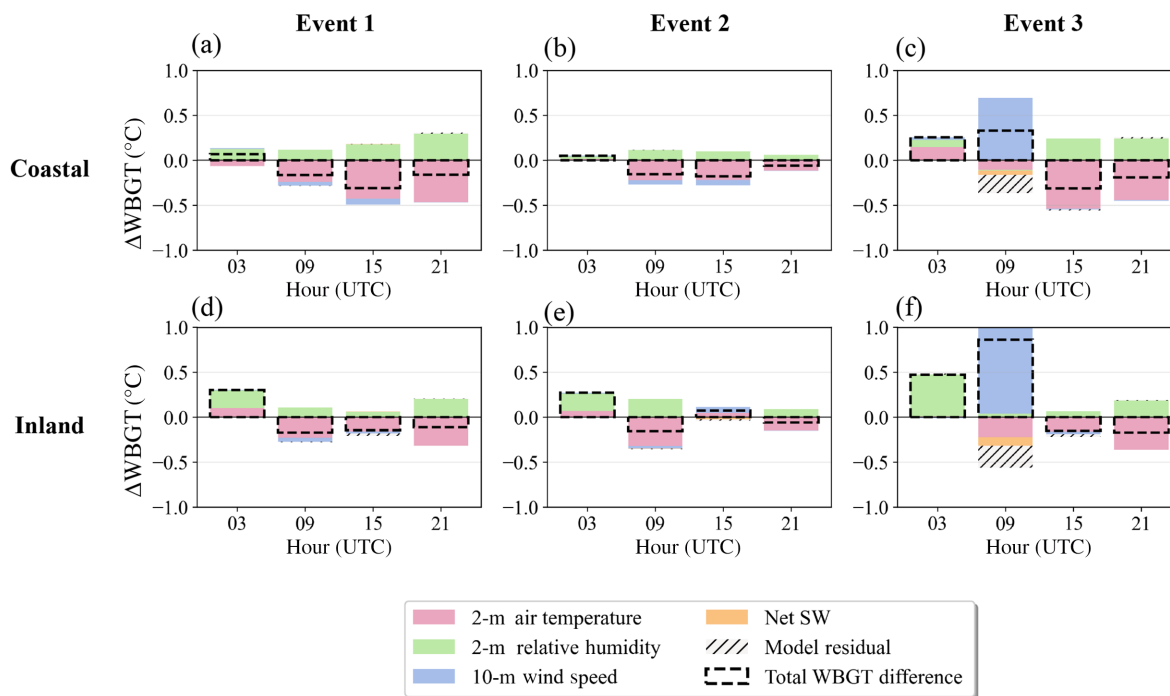


FIGURE 6 Factor contributions to wet-bulb globe temperature (WBGT) differences over the built-up grids due to the implementation of random water surface at four key time periods (0300, 0900, 1500, 2100 UTC) for (a)–(c) coastal and (d)–(f) inland for events 1–3. Coloured bars represent individual factor contributions: air temperature (pink), relative humidity (green), wind speed (blue), and net short-wave (SW) radiation (orange). Grey hatched bars show model residuals. Black dashed outlines indicate the total observed WBGT difference. Positive values indicate warming effects ($U7W3 > U1W0$), whereas negative values indicate cooling effects ($U7W3 < U1W0$). [Colour figure can be viewed at wileyonlinelibrary.com]

trade-off inherent in heat stress dynamics. The analysis consistently shows that night-time periods (0300 UTC) exhibit warming effects ($+0.24^{\circ}\text{C}$ average), where both elevated air temperature and increased relative humidity over waterbodies synergistically contribute to positive WBGT differences, reflecting nocturnal heat release from water thermal mass and enhanced moisture evaporation. Morning hours (0900 UTC) display the highest variability, with pronounced event-dependent differences: events 1 and 2 show consistent cooling (-0.16°C on average), whereas event 3 demonstrates exceptional warming ($+0.60^{\circ}\text{C}$ average), creating the substantial overall variability. Afternoon periods (1500 UTC) demonstrate peak cooling potential (-0.17°C average), whereas evening hours (2100 UTC) maintain moderate cooling (-0.13°C average) with persistent air temperature dominance as urban surfaces begin radiative cooling. Across both coastal and inland domains, the dominant mechanism during daytime and early evening involves substantial WBGT reduction through lower air temperatures over water (negative pink bars), systematically counteracted by elevated relative humidity over water surfaces (positive green bars), creating the characteristic temperature–humidity competition that fundamentally governs the efficacy of urban

waterbody heat mitigation strategies throughout the diurnal cycle.

At 1500 UTC during event 2, the inland city exhibits an anomalous warming effect during the convective precipitation period, where three factors contribute to warming: elevated air temperature over water ($+0.065^{\circ}\text{C}$), reduced wind speeds over water compared with built-up areas (wind coefficient -0.49 with positive contribution $+0.33^{\circ}\text{C}$), and enhanced net short-wave radiation over water ($+0.09^{\circ}\text{C}$ with coefficient $+0.004$). This result is consistent with what we observed from the ΔT_2 . The warming pattern may result from differential precipitation effects, where urban scenarios experience more intense convective precipitation leading to stronger evaporative cooling and enhanced turbulent mixing through downdrafts, whereas water scenarios receive less precipitation and maintain relatively higher temperatures, weaker wind speeds, and greater solar radiation input.

At 0900 UTC during event 3, an exceptional warming exists in both coastal and inland domains, primarily driven by reduced wind speeds over waterbodies. The coastal area shows a wind coefficient of -1.7 with a positive contribution of $+0.75^{\circ}\text{C}$ and short-wave coefficient of -0.47 with a negative contribution of -0.04°C , whereas

the inland area exhibits a wind coefficient of -1.6 with a positive contribution of $+1.4^{\circ}\text{C}$ and a short-wave coefficient of -0.13 with a negative contribution of -0.04°C , indicating that significantly reduced wind speeds over the water case compared with the urban case are the dominant mechanism driving these exceptional morning warming effects.

4 | DISCUSSION ON THERMAL REGULATION MECHANISMS

4.1 | Land and water surface energy components

Figure 7 shows the energy balance components over the built-up (urban) area and the blue space (water surface) during event 1.

Over the built-up area, H is significantly greater than LE , and both remain positive throughout the day. In contrast, over the water surface, H is only slightly positive around sunrise (0300–0500 UTC) and becomes negative for the remainder of the day due to the lower surface temperature of the water surface. For most of the day, H is negative, indicating a stable boundary layer with a downward transfer of energy indicating the cooling of the air due to water surface. However, the absolute magnitude of H is less than 6% of R_{net} and therefore is not a dominant mechanism of cooling and does not significantly influence the atmospheric temperature.

LE over the water surface is higher at night than during the day, which is the opposite of the pattern observed over land. Furthermore, at 1200 UTC, LE is only about 5% of the R_{net} , indicating most of the net radiation is utilized to convert the storage energy of water. This diurnal behaviour of H and LE is consistent with findings

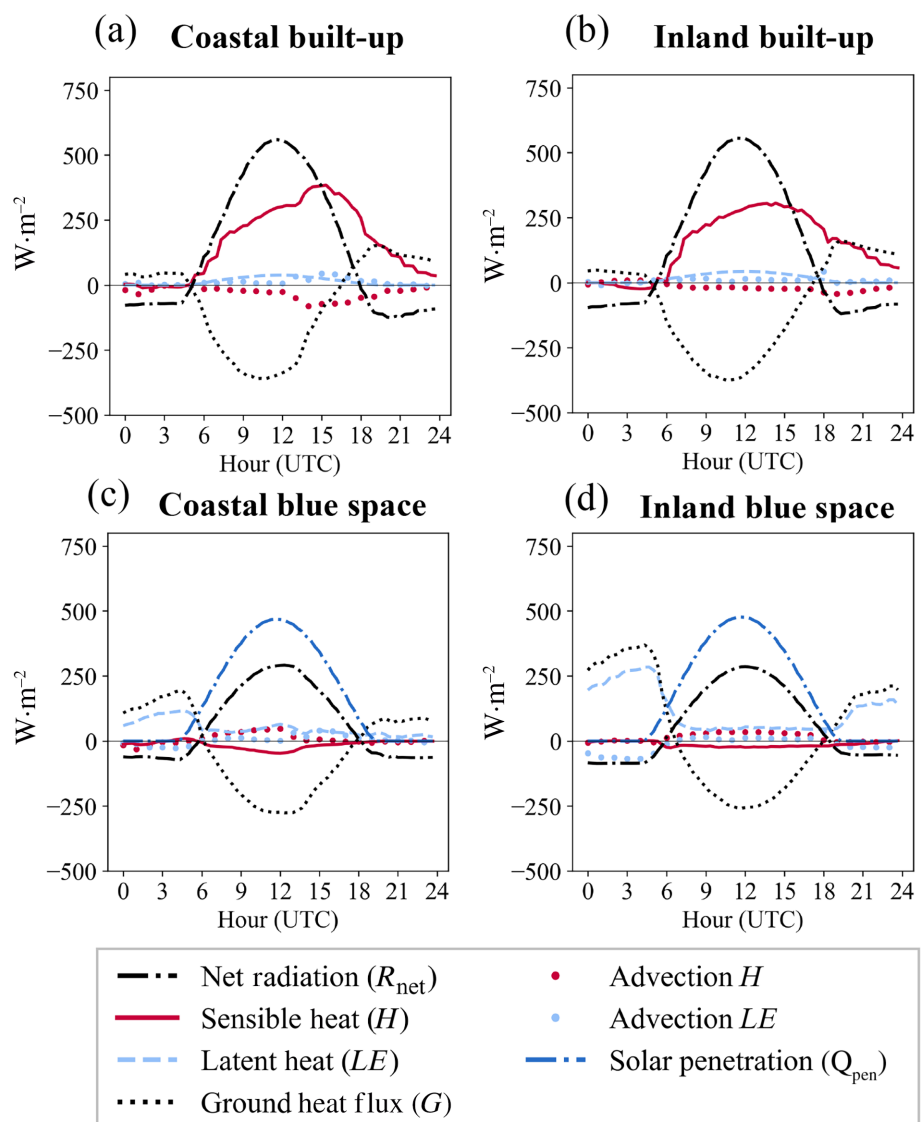


FIGURE 7 Diurnal profile of surface energy balance components and net horizontal mean advection (in the lowest 25 m of the atmosphere) of the simulation at coastal and inland cities (a, b) over the built-up area and (c, d) over the blue spaces during event 1. [Colour figure can be viewed at [wileyonlinelibrary.com](https://onlinelibrary.wiley.com)]

by Theeuwes *et al.* (2013), who reported similar patterns over an urban lake using WRF simulations under stable atmospheric conditions in early summer. However, an important point to note here is that the variation of LE over water surfaces in WRF is extremely sensitive to the modelling choices, specifically roughness and stability correction functions influencing the friction velocity and aerodynamic resistance. Therefore, these results need further analysis. Though the roughness values used in the WRF-Lake model might be appropriate for large lakes and open blue spaces, the same may not be true for urban blue spaces such as canals, which are situated in regions of higher turbulence where the assumptions of horizontal homogeneity are not generally valid. In summary, our results show that, with the current modelling choices of the lake model in WRF, both H and LE over water surface are not dominant and most of the input energy enters the water and is used in changing the internal energy of the water, which changes the water temperature. We perform a deeper analysis of the variation of LE over water surface and the limitations of the WRF-Lake model for urban blue-space modelling in Section 4.3.

In contrast to the water surface, H is the dominant energy sink over the built-up areas, with H accounting for close to 50% of the R_{net} at peak solar heating. For the coastal city in built-up areas, the red solid line representing H shows a sharp increase starting at 1300 UTC, peaking around 1500 UTC (Figure 7a). We find that this sharp increase in H is caused by the near-surface horizontal advection of sensible and latent heat fluxes (H_{adv} and LE_{adv}). In built-up areas, H_{adv} is typically negative, and positive over blue spaces. Negative H_{adv} over built-up areas indicates that the heat is lost from the air above the surface, indicating the cooling effect caused by the nearby water surfaces. Similarly, positive H_{adv} over the water surface indicates energy gained by the air above the surface of water, indicating the heat transfer from built-up areas to the water surface. H_{adv} is nearly 10% of the total R_{net} at 1500 UTC, indicating this is the dominant mechanism of lateral heat transfer between urban and blue spaces. In contrast, the magnitude of LE_{adv} is relatively small, generally contributing less than $10 \text{ W} \cdot \text{m}^{-2}$ to the daily mean. We elaborate on the mechanism and effect of advection as the dominant cooling mechanism by the urban blue spaces in Section 4.2.

The ground heat flux G over both surfaces exhibits a clear diurnal cycle: it is negative during the day (indicating heat storage) and positive at night (indicating heat release), with a pronounced negative peak around midday. During the day, G is directed downward, meaning that a substantial portion of the absorbed radiation is stored in the surface. At night, this stored heat is gradually released. Notably, the timing of this release differs between surfaces:

the built-up area releases more heat in the early evening, whereas the blue space releases more in the late evening.

Surface R_{net} is higher over the urban surface than over the water surface, primarily due to the penetration of the water. The radiation penetration term Q_{pen} does not participate in the surface energy balance of a waterbody. It represents the portion of incoming short-wave solar radiation that passes through the water surface and continues downward into the water column and is finally absorbed. Unlike other energy fluxes that are absorbed or reflected near the surface, this term accounts for energy that contributes to subsurface heating, influencing thermal stratification and internal mixing processes. It is only active during the daytime, when solar radiation is present, and its magnitude depends on factors such as water clarity, solar angle, and surface conditions. By transferring energy away from the surface, the penetration term effectively reduces the amount of heat available at the surface, playing a crucial role in the vertical distribution of heat within aquatic systems. At night, the majority of the heat released from the waterbody (represented by positive G) is dissipated through LE , with the remainder balanced by radiative cooling (negative R_{net}) and a small warming effect (positive H). In contrast, the radiation that penetrated the water surface is completely absorbed and is not released during the night, indicating that this energy is stored in the water and contributes to increase in the subsurface water temperature; this will be elaborated in Section 4.3.

4.2 | Role of horizontal advection in heat exchange between blue space and built-up areas

The presence of differentially heated thermal surfaces gives rise to thermal circulations that are similar to land-sea breezes (Allouche *et al.*, 2023). According to (Cuxart *et al.*, 2016), in the presence of thermal heterogeneity, persistent advective fluxes are found dominant at hectometric and decametre scales, and give rise to thermal circulations that contribute to the surface energy balance. These studies show that the presence of differentially heated surfaces next to each other gives rise to persistent thermal circulations or advective fluxes. In our study, the presence of urban blue spaces creates thermal heterogeneity and, consequently, persistent advective fluxes, modifying the surface energy balance. In Figure 7, H_{adv} was presented with the advection calculated as the net horizontal mean advective flux between the surface and the first mass point in WRF (approximately the lowest 25 m of the atmosphere in our simulations). In the previous section, we observed that H is influenced by the

horizontal advection over urban areas, with H_{adv} acting as the dominant mechanism of horizontal heat transfer.

Avisar and Schmidt (1998), based on idealized large-eddy simulations, report that in the presence of differential heating with regions where sensible heat flux varies horizontally, a large amount of heat is released into the atmosphere from the surface where the H is maximum, which results in an unstable convective boundary layer. The surface where H is minimum limits the development of boundary layer; therefore, the boundary layer remains shallow. The differential heating generated by the gradient of H gives rise to a horizontal pressure gradient, with regions of high H having lower surface pressure compared than regions of low H having a higher surface pressure. This difference in surface pressure generates a flow of air from relatively cold to relatively warm areas.

In our simulations, during daytime, H_{adv} is typically negative, indicating that more sensible heat H is being transported out of the grid cell due to advection. This reduces the near-surface air temperature, causing an increase in the difference between surface and air temperatures, which results in a sharp increase of H over built-up areas (Figure 7a). The corresponding H_{adv} follows a similar temporal pattern but with negative values, confirming the outward flow of warm air from built-up areas towards the blue space. Over water surfaces (blue space), the horizontal advection of sensible heat H_{adv} during the daytime exhibits positive values, whereas the surface sensible heat flux H is negative. This occurs because the water surface typically has a lower temperature than the surrounding land, resulting in a net inflow of sensible heat into the grid cell (positive H_{adv}). As shown in Figure 7c,d,

the magnitudes of H_{adv} and H are comparable, indicating that horizontal advection is the primary mechanism responsible for the cooling effect of the water surface on the surrounding land.

To further investigate the role of near-surface advection, Figure 8 presents the diurnal variation of H_{adv} difference between the U7W3r case and the CTL (ΔH_{adv}). The ΔH_{adv} represents the horizontal sensible heat advection among the urban and water surfaces, effectively isolating the local advection signal from the broader regional background. The red lines in Figure 8 represent ΔH_{adv} over built-up areas, and the blue lines correspond to the results over blue spaces in the cities. As with H_{adv} , the positive ΔH_{adv} values represent more sensible heat coming in than going out, which usually occurs over the water surfaces, indicating the surrounding built-up area warms the water surface through advection. On the other hand, the negative ΔH_{adv} value is usually shown over the built-up area, indicating that the surroundings cool the built-up area through advection.

In the coastal city (solid lines), the peak of ΔH_{adv} over the water occurs around 1200 UTC. This represents that blue spaces are warmed up by the surroundings approximately $50 \text{ W} \cdot \text{m}^{-2}$ during events 1 and 2, and about $42 \text{ W} \cdot \text{m}^{-2}$ in event 3. Over the built-up area in the coastal city, ΔH_{adv} exhibits negative peaks around 1800 UTC. This indicates that the advection cooling in built-up areas from surrounding blue space is strong in the late afternoon to early evening, with values ranging from 30 to $25 \text{ W} \cdot \text{m}^{-2}$. In the inland city (dashed lines), the ΔH_{adv} over the water is slightly lower than in the coastal city, primarily due to weaker horizontal wind speeds. However,

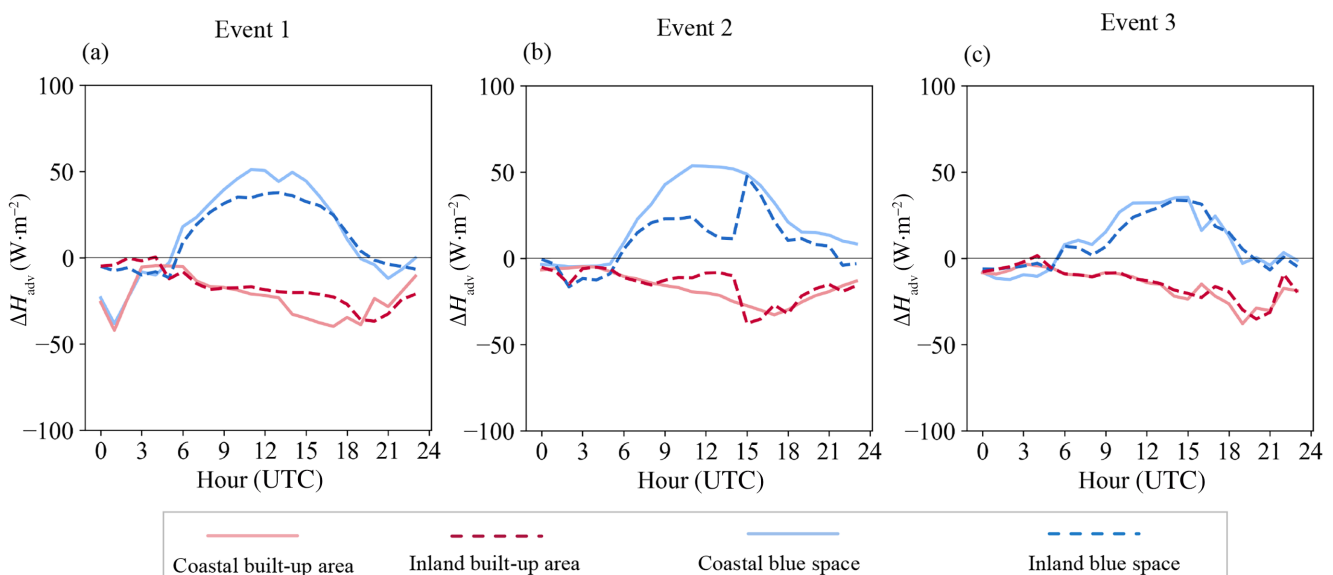


FIGURE 8 Diurnal profile of the horizontal advection difference between U7W3r and CTL (ΔH_{adv}) at coastal and inland cities during (a) event 1, (b) event 2, and (c) event 3. [Colour figure can be viewed at [wileyonlinelibrary.com](https://onlinelibrary.wiley.com/doi/10.1002/qj.70128)]

in event 3, the values in both cities are comparable, which corresponds to similar wind speeds observed during that event. [Supporting Information Figure S6](#) shows the diurnal variation of wind speed at 10 m on a spatial average. In [Figure 8b](#), the results for the inland city show a sudden fluctuation at 1400–1700 UTC, when the convective rainfall occurred. The amount of incoming sensible heat from the water surface exceeds the outgoing amount from the built-up area. This suggests that the cooling effect originating from the blue space extends beyond the urban area, influencing regions outside the city. This observation is consistent with the spatial patterns shown in [Figure 4](#).

[Figure 9](#) illustrates the spatial distribution of ΔH_{adv} in the cities at 1200 UTC. The reddish colours indicate areas of positive ΔH_{adv} , predominantly covering the blue space (water surface). In [Figure 9a,b](#), darker blue shades represent strongly negative H_{adv} values, which appear in grid cells adjacent to the reddish areas and gradually weaken in a specific direction—aligned with the

prevailing wind. This pattern is particularly evident under stronger wind conditions. For instance, in the coastal city at 1200 UTC, the spatially averaged near-surface wind speed over built-up areas exceeds $6 \text{ m} \cdot \text{s}^{-1}$ ([Supporting Information Figure S6](#)). The spatial variation clearly shows that built-up areas lose heat and the blue spaces gain heat due to advection.

4.3 | Performance of WRF-Lake parametrization over urban blue spaces

As shown in [Figure 7](#) during daytime (0600–1800 UTC), LE is low in magnitude over both built-up and blue space with values as low as $20\text{--}60 \text{ W} \cdot \text{m}^{-2}$. Owing to the low values of LE , evaporative cooling does not contribute significantly to cooling over built-up areas in our simulations. As elaborated in [Section 4.2](#), H_{adv} over blue space is the dominant mechanism of horizontal transfer of the cooling

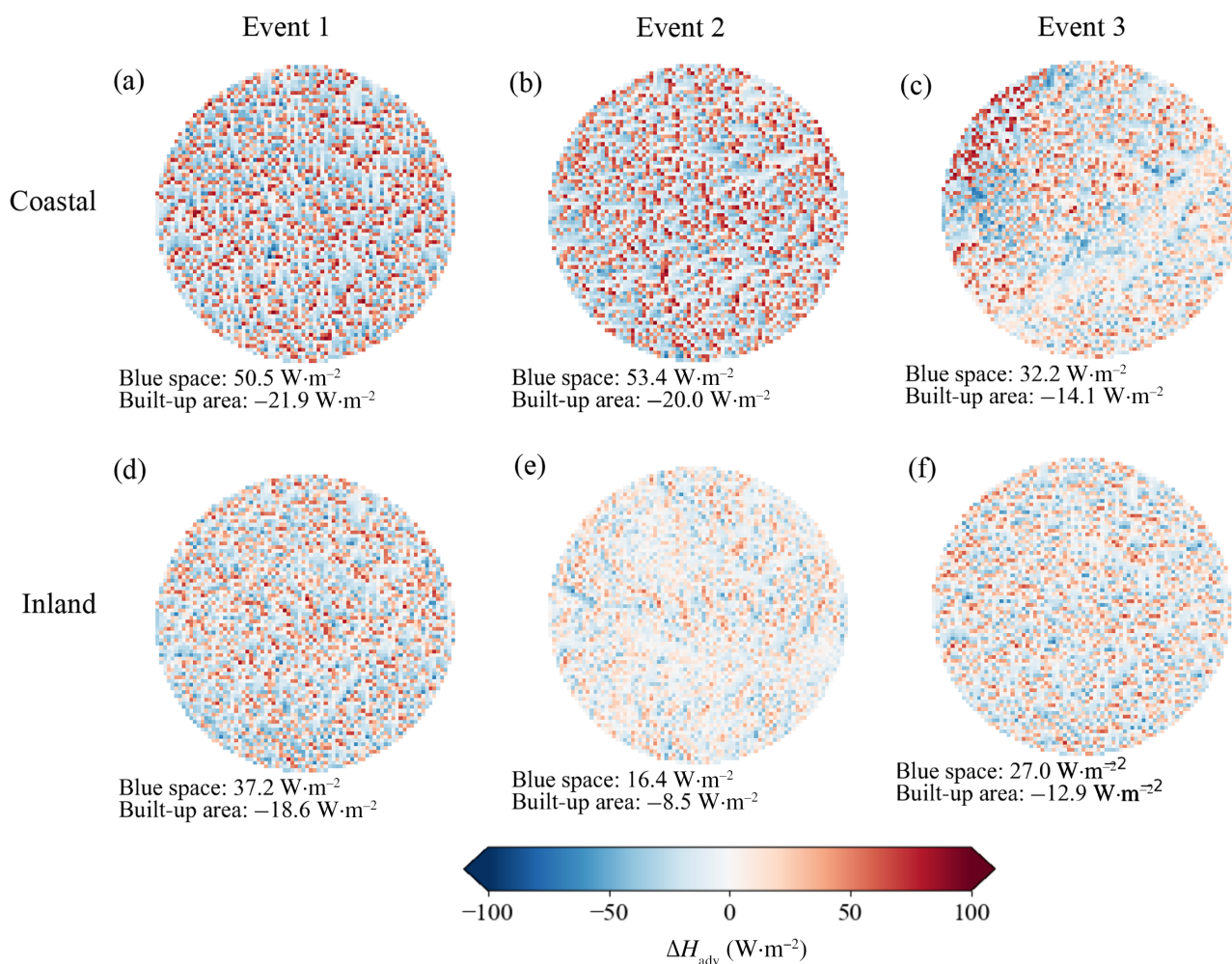


FIGURE 9 Spatial distribution of the horizontal advection difference ΔH_{adv} at 1200 UTC, representing the effect of built-up areas and randomly placed blue spaces. Results are shown for (a, d) event 1, (b, e) event 2, and (c, f) event 3, with (a)–(c) corresponding to coastal cities and (d)–(f) to inland cities. [Colour figure can be viewed at [wileyonlinelibrary.com](https://onlinelibrary.wiley.com/doi/10.1002/qj.70128)] <https://onlinelibrary.wiley.com/doi/10.1002/qj.70128>

effect over built-up areas. In the absence of significant LE , H_{adv} depends mostly on the temperature gradient due to the low water surface temperature. Figure 7c,d shows that LE over the blue space exhibits an unusual diurnal variation, with higher values during the night-time compared with the daytime. Similar variations have been reported from WRF simulations over Amsterdam by Theeuwes *et al.* (2013). We hypothesize that this unusual variation may be related to the modelling choices made in lake module in WRF and elaborate on this possibility herewith.

LE ($W \cdot m^{-2}$) is modelled in the WRF-Lake model with in which L_v is the latent heat of vaporization of water, ρ_{atm} ($kg \cdot m^{-3}$) is the air density, r_{aw} ($s \cdot m^{-1}$) is aerodynamic resistance, q ($kg \cdot kg^{-1}$) represents the specific humidity, “sat” means saturated, and “atm” means atmosphere, and n represents the current time step. The lake surface temperature T_{lake} ($^{\circ}C$) represents an infinitesimal interface layer between the top resolved lake layer and the aerodynamic atmosphere and is solved simultaneously with the surface fluxes. From Equation (8), it is clear that the magnitude of LE in WRF depends largely on two terms: (a) the specific humidity difference between the water surface and the air, and (b) the friction velocity u^* . Figure 10a–c shows the humidity difference between the water surface and the air. Large differences contribute to large LE . The difference is larger in the inland location than the coastal region, and both reach their peaks at 1500 UTC. However, LE does not follow the pattern of undersaturation over the blue space. Figure 10d–f shows the friction velocity over the urban built-up area and over the blue space. The friction velocity is very low over the blue space (blue lines), and the pattern is very similar to the pattern of LE over the blue space. Therefore, the small LE amount appears to be directly related to the small friction velocity during the daytime. The friction velocity is less than $0.1 m \cdot s^{-1}$ during the daytime in all three events, which in turn indicates lower turbulent mixing, and therefore lower LE .

$$LE = -\frac{L_v \rho_{atm}}{r_{aw}} \times \left[q_{atm} - q_{sat}^{T_{lake}} - \frac{\partial q_{sat}^{T_{lake}}}{\partial T_{lake}} (T_{lake}^{n+1} - T_{lake}^n) \right], \quad (8)$$

We hypothesize that a major factor contributing to low u^* over water surfaces is the low surface roughness of blue spaces assumed in the lake model. In WRF, a roughness length of 0.001 m is used for unfrozen lakes (Gu *et al.*, 2016). Though this low roughness length is appropriate for large open natural water surfaces, it may not accurately represent small urban blue spaces embedded within heterogeneous urban landscapes. The roughness parametrization is in accordance with Monin–Obukhov

similarity theory. In urban areas, owing to high urban roughness, the wind flow is associated with higher turbulence compared with homogeneous areas such as open water lake or cropland. This suggests that blue spaces located in urban areas may experience enhanced turbulence from surrounding urban elements that is not captured by the current parametrization. In the current WRF-Lake model, this roughness length is applied uniformly, potentially underestimating surface–atmosphere interactions in urban blue spaces (Gu *et al.*, 2015; Gu *et al.*, 2016). The friction velocity over built-up areas (red-dish lines in Figure 10d–f) is significantly higher than over adjacent urban blue spaces (blue lines), suggesting that the current modelling approach may not adequately capture the unique surface energy dynamics of small urban blue spaces.

The unusually low LE observed over the blue space in our simulations leads to unrealistically high storage fluxes in that region. Woolway *et al.* (2020) pointed out that, during the heatwave days in 2018, the maximum lake surface temperature over natural lakes is around $2.4^{\circ}C$ higher than the period base. However, Figure 10g–i illustrates lake surface temperature T_{lake} ($^{\circ}C$) in our simulations, which increases by approximately $2.0^{\circ}C$ over the course of a single hot summer day. If such conditions persist over multi-day heatwave events, the model projects a continued rise in water temperature that may be unreasonably high compared with observations (Wang *et al.*, 2024; Woolway *et al.*, 2020).

These unexpected LE and water temperature patterns raise important questions about model representation of urban blue spaces. Model validation for small, shallow urban blue spaces is beyond the scope of this idealized study. Nevertheless, we offer several hypotheses to explain the observed behaviour. The low surface roughness parametrization (0.001 m) in the WRF-Lake model, designed for large open waterbodies, may not capture the enhanced turbulence that urban roughness elements generate over adjacent water surfaces. This could lead to underestimation of friction velocity and, consequently, suppressed latent heat fluxes. If this hypothesis holds, a more accurate representation of LE would likely result in lower air temperatures over blue spaces and enhanced horizontal advection of sensible heat H_{adv} , further amplifying the cooling effect. The results presented here could therefore represent a lower bound of the actual cooling potential of urban blue spaces.

However, the actual mechanisms governing energy exchange over small urban waterbodies may be more complex than our hypothesis suggests, potentially involving interactions between shallow water thermal dynamics, urban-induced turbulence, and lateral boundary effects that are not well represented in current

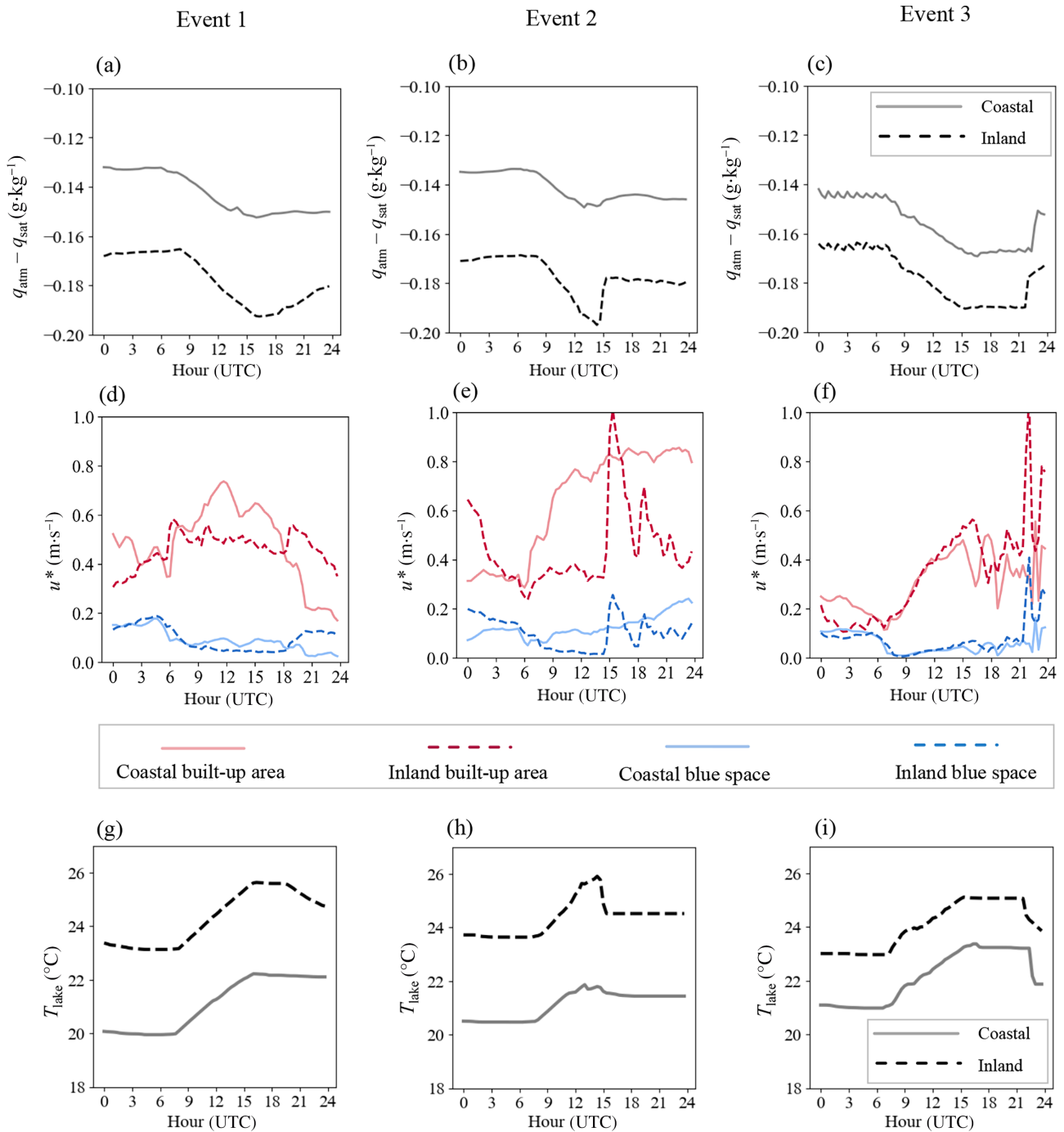


FIGURE 10 Specific humidity difference between the near-surface atmosphere and the water surface ($q_{\text{atm}} - q_{\text{sat}}$) during (a) event 1, (b) event 2, and (c) event 3 in case U7W3r. Friction velocity u_* over urban built-up areas and water surfaces is shown during (d) event 1, (e) event 2, and (f) event 3 in the same scenario. Lake surface temperature T_{lake} is presented during (g) event 1, (h) event 2, and (i) event 3, also for case U7W3r. [Colour figure can be viewed at [wileyonlinelibrary.com](https://onlinelibrary.wiley.com/doi/10.1002/qj.70128)]

parametrization schemes. Addressing these uncertainties requires coordinated efforts from the urban climate community in two parallel directions: first, establishing observational campaigns to measure energy fluxes over small urban waterbodies, which would provide essential validation data currently lacking in the literature (Van Der Meulen *et al.*, 2023); and second,

developing improved parametrization schemes that incorporate physics appropriate for shallow urban blue spaces embedded within rough urban environments. Progress on both fronts is essential for advancing the accuracy of urban hydro-meteorological simulations and understanding the true cooling potential of urban blue-space infrastructure.

5 | CONCLUSIONS

This study investigated the role of urban blue spaces in regulating the thermal environment during three extreme heat events in northwestern Europe, using high-resolution (100 m) WRF idealized simulations. We evaluated their influence on 2-m air temperature and the WBGT thermal comfort index, capturing both localized and city-wide effects. We also analysed the surface energy balance to obtain an understanding of the physical mechanisms driving the thermal regulation by blue spaces at neighbourhood scale and the suitability of WRF-Lake parametrization in modelling the effect of urban blue spaces.

Our findings suggest that urban blue spaces present cooling effects on air temperature with distinct temporal and spatial patterns across three hot events. Daily mean cooling ranged from -0.1°C to -0.4°C , with peak effectiveness during morning hours (0600–0800 UTC) achieving reductions up to -1.0°C in coastal areas based on simulations of idealized urban landscape. Wind speed emerged as the primary control on cooling extent, with general to moderate winds ($4.7\text{--}5.8\text{ m}\cdot\text{s}^{-1}$) propagating cooling effects 20–25 km (three times to the city radius) downwind through shallow planetary boundary layers, whereas light air winds ($1.2\text{ m}\cdot\text{s}^{-1}$) limited cooling to approximately 3 km. Spatial configuration significantly influenced cooling distribution, with randomly distributed waterbodies creating more homogeneous patterns compared with canal configurations. Coastal cities exhibited enhanced cooling during sea breeze events, whereas inland cities showed complex interactions with urban-induced convection.

The thermal comfort analysis, represented by WBGT, revealed a fundamental temperature–humidity trade-off governing heat stress mitigation. Factor analysis (mean $R^2 = 0.93$) identified air temperature cooling as the primary beneficial mechanism (50.3% contribution), systematically counteracted by increased relative humidity (42.3% contribution). This competition created distinct diurnal patterns: afternoon periods showed peak WBGT cooling potential (-0.17°C), whereas night-time exhibited warming effects ($+0.24^{\circ}\text{C}$) due to nocturnal heat release and moisture evaporation. These findings underscore that blue-space effectiveness depends critically on time of day, meteorological conditions, and spatial configuration, with wind speed playing a pivotal role in determining whether temperature reductions or humidity increases dominate the overall heat stress response. Urban planning strategies should account for these complex dynamics rather than assuming uniform cooling benefits across all conditions.

A key contribution of this study is the identification and quantification of the heat exchange

mechanism between built-up areas and adjacent blue spaces. Unlike previous studies using coarser-resolution WRF simulations (e.g., 1 km), which cannot resolve neighbourhood-scale processes, our hectometric-scale simulations capture near-surface neighbourhood-scale horizontal advection. This mechanism facilitates the mixing of cooler air from blue spaces with warmer urban air and is identified as the dominant process through which blue spaces exert their thermal regulatory influence. Around midday, blue spaces exhibited a cooling potential of approximately $50\text{ W}\cdot\text{m}^{-2}$. This effect is further amplified by the cooling due to latent heat flux due to evaporation of water in the blue spaces. However, we find that the latent heat flux is influenced largely by the turbulence in the urban area.

Despite the advantages of high-resolution modelling, we identified limitations in the WRF-Lake model, particularly in simulating latent heat fluxes over shallow urban blue spaces. The current WRF-Lake model, which uses low roughness lengths appropriate for large, deep, open waterbodies, produces unexpectedly low turbulent heat fluxes, leading to unrealistic energy balance partitioning and water temperature increases. We hypothesize that this parametrization may underestimate friction velocities and fail to capture the enhanced turbulence generated by urban roughness elements, potentially leading to underestimation of the cooling effects of urban blue spaces. However, this hypothesis remains speculative. Without observational data from urban water surfaces, we cannot confirm whether the model actually underestimates or overestimates cooling effects, nor can we verify the mechanisms we propose to explain model behaviour. This underlines the need for field campaigns to measure flux balance in urban blue spaces.

The evaporation dynamics of small urban blue spaces remain underresearched, with limited empirical data and analytical studies available. Similarly, the energy balance of urban blue spaces has received little attention. This gap is partly due to the complexity of urban environments, which makes eddy covariance techniques unsuitable for accurately measuring sensible and latent heat fluxes in small, shallow urban blue spaces such as canals. Traditional flux measurement techniques cannot isolate contributions from individual land-use types embedded within heterogeneous urban landscapes. Moreover, the parametrization schemes used in current physically based urban simulation tools have not been sufficiently validated for urban blue-space settings. Addressing the identified limitations likely requires developing new parametrization schemes that include more comprehensive and physically appropriate representations of urban–water interactions, such as the influence of urban roughness on water

surface turbulence, the effects of shallow depth on thermal dynamics, and the exchange processes at urban–water boundaries (Chen *et al.*, 2025).

These findings underscore the need for parallel research efforts. First, observational campaigns focused on the energy balance of shallow urban blue spaces are essential to establish ground truth data and validate model performance. Second, developing enhanced modelling tools with improved parametrization schemes specifically tailored to the unique characteristics of small, shallow urban blue spaces is necessary to improve the accuracy of urban hydro-meteorological simulations. The current WRF-Lake module and Noah land-surface model exhibit significant limitations in representing turbulent heat fluxes and moist transport processes over complex urban landscapes. With insufficient observational data to guide and validate model improvements, progress on both fronts will remain limited.

Finally, we emphasize that this study employs an idealized modelling approach to isolate and understand fundamental physical mechanisms. Although our simulation locations correspond to real urban areas in north-western Europe, the controlled land-use configurations we designed for systematic comparison do not exist in reality and cannot be directly validated against observations. The strength of this approach lies in identifying dominant mechanisms, revealing process relationships, and understanding how meteorological conditions and spatial configurations influence cooling effectiveness, insights that would be difficult to obtain from complex real-world settings. However, the specific quantitative cooling magnitudes we report should be interpreted as results from our controlled idealized scenarios rather than precise predictions for actual cities. Applying these findings to real-world urban planning decisions requires follow-up studies using realistic land-use configurations validated against observations. Nevertheless, the mechanistic insights and model limitations we identify provide valuable contributions to advancing urban climate science and informing the development of more sophisticated modelling approaches for urban blue spaces.

ACKNOWLEDGEMENTS

We acknowledge feedback from three anonymous reviewers for their constructive feedback on the earlier version of the manuscript.

CONFLICT OF INTEREST STATEMENT

One of the authors is an associate editor of the *Quarterly Journal of the Royal Meteorological Society*. The authors have no other competing interests to declare.

DATA AVAILABILITY STATEMENT

The ERA5 reanalysis data used in this study are publicly available from the European Centre for Medium-Range Weather Forecasts at <https://www.ecmwf.int/en/forecasts/dataset/ecmwf-reanalysis-v5>. The simulation results generated during the current study are available from the corresponding author upon reasonable request. The PyWBGT package that works for WRF outputs is publicly available at GitHub (PyWBGT_WRF GitHub Repository).

ORCID

Xuan Chen  <https://orcid.org/0000-0001-5307-2217>

Arjan Droste  <https://orcid.org/0000-0003-0218-5160>

Gert-Jan Steeneveld  <https://orcid.org/0000-0002-5922-8179>

REFERENCES

- Allouche, M., Bou-Zeid, E. & Iipponen, J. (2023) The influence of synoptic wind on land–sea breezes. *Quarterly Journal of the Royal Meteorological Society*, 149, 3198–3219.
- Ampatzidis, P. & Kershaw, T. (2020) A review of the impact of blue space on the urban microclimate. *Science of the Total Environment*, 730, 139068.
- Avisar, R. & Schmidt, T. (1998) An evaluation of the scale at which ground-surface heat flux patchiness affects the convective boundary layer using large-eddy simulations. *Journal of the Atmospheric Sciences*, 55, 2666–2689.
- Beck, H.E., McVicar, T.R., Vergopolan, N., Berg, A., Lutsko, N.J., Dufour, A. et al. (2023) High-resolution (1 km) Köppen-Geiger maps for 1901–2099 based on constrained CMIP6 projections. *Scientific Data*, 10, 724. Available from: <https://www.nature.com/articles/s41597-023-02549-6>
- Broxton, P.D., Zeng, X., Sulla-Menashe, D. & Troch, P.A. (2014) A global land cover climatology using MODIS data. *Journal of Applied Meteorology and Climatology*, 53(6), 1593–1605.
- Chakraborty, T., Venter, Z.S., Qian, Y. & Lee, X. (2022) Lower urban humidity moderates outdoor heat stress. *AGU Advances*, 3, e2022AV000729. Available from: <https://doi.org/10.1029/2022AV000729>
- Chen, F. & Dudhia, J. (2001) Coupling an advanced land surface–hydrology model with the Penn State–NCAR MM5 modeling system. Part I: model implementation and sensitivity. *Monthly Weather Review*, 129(4), 569–585.
- Chen, X., van der Werf, J.A., Droste, A., Coenders-Gerrits, M. & Uijlenhoet, R. (2025) Barriers to urban hydrometeorological simulation: a review. *Hydrology and Earth System Sciences*, 29(15), 3447–3480.
- Ching, J., Mills, G., Bechtel, B., See, L., Feddema, J., Wang, X. et al. (2018) WUDAPT: an urban weather, climate, and environmental modeling infrastructure for the anthropocene. *Bulletin of the American Meteorological Society*, 99(9), 1907–1924.
- City of Amsterdam, C. O. A. (2025) *Policy: water and boating*. Amsterdam, the Netherlands: Gemeente Amsterdam. Available from: <https://www.amsterdam.nl/en/policy/policy-water-boating/> [Accessed 19th June 2025].
- Cuxart, J., Wrenger, B., Martínez-Villagrana, D., Reuder, J., Jonassen, M.O., Jiménez, M.A. et al. (2016) Estimation of the

- advection effects induced by surface heterogeneities in the surface energy budget. *Atmospheric Chemistry and Physics*, 16, 9489–9504.
- Ding, W. & Chen, H. (2024) Investigating the microclimate impacts of blue–green space development in the urban–rural fringe using the WRF-UCM model. *Urban Climate*, 54, 101865.
- Dudhia, J. (1989) Numerical study of convection observed during the winter monsoon experiment using a mesoscale two-dimensional model. *Journal of Atmospheric Sciences*, 46(20), 3077–3107.
- European Environment Agency. (2025) Hot Days. <https://climate-adapt.eea.europa.eu/en/metadata/indicators/hot-days>
- Forster, A., Augros, C. & Masson, V. (2024) Urban influence on convective precipitation in the Paris region: Hectometric ensemble simulations in a case study. *Quarterly Journal of the Royal Meteorological Society*, 150, 3028–3051. Available from: <https://doi.org/10.1002/qj.4749>
- Fricke, L., Legg, R. & Kabisch, N. (2024) Impact of blue spaces on the urban microclimate in different climate zones, daytimes and seasons – a systematic review. *Urban Forestry & Urban Greening*, 101, 128528.
- Gao, S., Chen, Y., Chen, D., He, B., Gong, A., Hou, P. et al. (2024) Urbanization-induced warming amplifies population exposure to compound heatwaves but narrows exposure inequality between global North and South cities. *NPJ Climate and Atmospheric Science*, 7, 1–10.
- García-Herrera, R., Díaz, J., Trigo, R.M., Luterbacher, J. & Fischer, E.M. (2010) A review of the European summer heat wave of 2003. *Critical Reviews in Environmental Science and Technology*, 40(4), 267–306. Available from: <https://doi.org/10.1080/10643380802238137>
- Göbel, M., Serafin, S. & Rotach, M.W. (2022) Numerically consistent budgets of potential temperature, momentum, and moisture in Cartesian coordinates: application to the WRF model. *Geoscientific Model Development*, 15, 669–681.
- Gu, H., Jin, J., Wu, Y., Ek, M.B. & Subin, Z.M. (2015) Calibration and validation of lake surface temperature simulations with the coupled WRF-lake model. *Climatic Change*, 129, 471–483. Available from: <https://doi.org/10.1007/s10584-013-0978-y>
- Gu, H., Ma, Z. & Li, M. (2016) Effect of a large and very shallow lake on local summer precipitation over the Lake Taihu basin in China. *Journal of Geophysical Research: Atmospheres*, 121, 8832–8848. Available from: <https://doi.org/10.1002/2015JD024098>
- Guo, S., Wang, F., Zhu, D., Ni, G. & Chen, Y. (2022) Evaluation of the WRF-lake model in the large dimictic reservoir: comparisons with field data and another water temperature model. *Journal of Hydrometeorology*, 23, 1227–1244.
- Hathway, E.A. & Sharples, S. (2012) The interaction of rivers and urban form in mitigating the Urban Heat Island effect: a UK case study. *Building and Environment*, 58, 14–22.
- Hersbach, H., Bell, B., Berrisford, P., Hirahara, S., Horányi, A., Muñoz-Sabater, J. et al. (2020) The ERA5 global reanalysis. *Quarterly Journal of the Royal Meteorological Society*, 146, 1999–2049. Available from: <https://doi.org/10.1002/qj.3803>
- Hong, S.-Y., Noh, Y. & Dudhia, J. (2006) A new vertical diffusion package with an explicit treatment of entrainment processes. *Monthly Weather Review*, 134(9), 2318–2341.
- Jacobs, C., Klok, L., Bruse, M., Cortesão, J., Lenzholzer, S. & Kluck, J. (2020) Are urban water bodies really cooling? *Urban Climate*, 32, 100607.
- Jiménez, P.A., Dudhia, J., González-Rouco, J.F., Navarro, J., Monávez, J.P. & García-Bustamante, E. (2012) A revised scheme for the WRF surface layer formulation. *Monthly Weather Review*, 140(3), 898–918.
- Kong, Q. & Huber, M. (2022) Explicit calculations of wet-bulb globe temperature compared with approximations and why it matters for labor productivity. *Earth's Future*, 10, e2021EF002334. Available from: <https://doi.org/10.1029/2021EF002334>
- Koopmans, S., van Haren, R., Theeuwes, N., Ronda, R., Uijlenhoet, R., Holtslag, A.A.M. et al. (2023) The set-up and evaluation of fine-scale data assimilation for the urban climate of Amsterdam. *Quarterly Journal of the Royal Meteorological Society*, 149, 171–191. Available from: <https://doi.org/10.1002/qj.4401>
- Kusaka, H., Kondo, H., Kikegawa, Y. & Kimura, F. (2001) A simple single-layer urban canopy model for atmospheric models: comparison with multi-layer and slab models. *Boundary-Layer Meteorology*, 101, 329–358. Available from: [10.1023/A:1019207923078](https://doi.org/10.1023/A:1019207923078).
- Liljegren, J.C., Carhart, R.A., Lawday, P., Tschopp, S. & Sharp, R. (2008) Modeling the wet bulb globe temperature using standard meteorological measurements. *Journal of Occupational and Environmental Hygiene*, 5, 645–655. Available from: <https://doi.org/10.1080/15459620802310770>
- Lilliefors, H.W. (1969) On the Kolmogorov-Smirnov test for the exponential distribution with mean unknown. *Journal of the American Statistical Association*, 64, 387–389. Available from: <https://doi.org/10.1080/01621459.1969.10500983>
- Lin, Y., Wang, Z., Jim, C.Y., Li, J., Deng, J. & Liu, J. (2020) Water as an urban heat sink: blue infrastructure alleviates urban heat island effect in mega-city agglomeration. *Journal of Cleaner Production*, 262, 121411.
- Margairaz, F., Pardyjak, E.R. & Calaf, M. (2020) Surface thermal heterogeneities and the atmospheric boundary layer: the relevance of dispersive fluxes. *Boundary-Layer Meteorology*, 175, 369–395.
- Matthews, T., Raymond, C., Foster, J., Baldwin, J.W., Ivanovich, C., Kong, Q. et al. (2025) Mortality impacts of the most extreme heat events. *Nature Reviews Earth & Environment*, 6, 193–210.
- Mlawer, E.J., Taubman, S.J., Brown, P.D., Iacono, M.J. & Clough, S.A. (1997) Radiative transfer for inhomogeneous atmospheres: RRTM, a validated correlated-k model for the longwave. *Journal of Geophysical Research: Atmospheres*, 102, 16663–16682. Available from: <https://doi.org/10.1029/97JD00237>
- Obulkasim, O., Zhang, S., Yang, X., Sun, L., He, Y. & Dai, Y. (2025) Understanding the performance of three 1-D lake models in simulating thermal dynamics of diverse water bodies in the Yangtze River Basin. *Journal of Hydrology*, 657, 133094.
- Pendergrass, A.G. (2018) What precipitation is extreme? *Science*, 360, 1072–1073. Available from: <https://doi.org/10.1126/science.aat1871>
- Peng, J., Cheng, X., Hu, Y. & Corcoran, J. (2022) A landscape connectivity approach to mitigating the urban heat island effect. *Landscape Ecology*, 37, 1707–1719. Available from: <https://doi.org/10.1007/s10980-022-01439-3>
- Ronda, R.J., Steeneveld, G.J., Heusinkveld, B.G., Attema, J.J. & Holtslag, A.A.M. (2017) Urban finescale forecasting reveals weather conditions with unprecedented detail. *Bulletin of the American Meteorological Society*, 98(12), 2675–2688.
- Rousi, E., Kornhuber, K., Beobide-Arsuaga, G., Luo, F. & Coumou, D. (2022) Accelerated western European heatwave trends linked to more-persistent double jets over Eurasia. *Nature*

- Communications*, 13, 3851. Available from: <https://www.nature.com/articles/s41467-022-31432-y>
- Skamarock, W., Klemp, J., Dudhia, J., Gill, D.O., Liu, A.Z., Berner, J. et al. (2019) A description of the advanced research WRF model version 4.1. <https://opensky.ucar.edu/islandora/object/%3A3888>
- Steenefeld, G.J., Koopmans, S., Heusinkveld, B.G. & Theeuwes, N.E. (2014) Refreshing the role of open water surfaces on mitigating the maximum urban heat island effect. *Landscape and Urban Planning*, 121, 92–96.
- Stephens, M.A. (1974) EDF statistics for goodness of fit and some comparisons. *Journal of the American Statistical Association*, 69, 730–737. Available from: <https://www.jstor.org/stable/2286009>
- Stewart, I.D. & Oke, T.R. (2012) Local climate zones for urban temperature studies. *Bulletin of the American Meteorological Society*, 93(12), 1879–1900.
- Subin, Z.M., Riley, W.J. & Mironov, D. (2012) An improved lake model for climate simulations: model structure, evaluation, and sensitivity analyses in CESM1. *Journal of Advances in Modeling Earth Systems*, 4(1). Available from: <https://doi.org/10.1029/2011MS000072>
- Theeuwes, N.E., Solcerová, A. & Steeneveld, G.J. (2013) Modeling the influence of open water surfaces on the summertime temperature and thermal comfort in the city. *Journal of Geophysical Research: Atmospheres*, 118, 8881–8896. Available from: <https://doi.org/10.1002/jgrd.50704>
- Thompson, G., Field, P.R., Rasmussen, R.M. & Hall, W.D. (2008) Explicit forecasts of winter precipitation using an improved bulk microphysics scheme. Part II: implementation of a new snow parameterization. *Monthly Weather Review*, 136(12), 5095–5115.
- Tominaga, Y., Sato, Y. & Sadohara, S. (2015) CFD simulations of the effect of evaporative cooling from water bodies in a micro-scale urban environment: validation and application studies. *Sustainable Cities and Society*, 19, 259–270.
- Tripathy, K.P. & Mishra, A.K. (2023) How unusual is the 2022 European compound drought and heatwave event? *Geophysical Research Letters*, 50, e2023GL105453. Available from: <https://doi.org/10.1029/2023GL105453>
- Van Der Meulen, E.S., Van de Ven, F.H., Van Oel, P.R., Rijnaarts, H.H. & Sutton, N.B. (2023) Improving suitability of urban canals and canalized rivers for transportation, thermal energy extraction and recreation in two European delta cities. *Ambio*, 52(1), 195–209.
- Wang, F., Ni, G., Riley, W.J., Tang, J., Zhu, D. & Sun, T. (2019) Evaluation of the WRF lake module (v1.0) and its improvements at a deep reservoir. *Geoscientific Model Development*, 12, 2119–2138.
- Wang, W. (2009) The influence of thermally-induced mesoscale circulations on turbulence statistics over an idealized urban area under a zero background wind. *Boundary-Layer Meteorology*, 131, 403–423. Available from: <https://doi.org/10.1007/s10546-009-9378-2>
- Wang, X., Shi, K., Qin, B., Zhang, Y. & Woolway, R.I. (2024) Disproportionate impact of atmospheric heat events on lake surface water temperature increases. *Nature Climate Change*, 14, 1172–1177.
- Woolway, R.I., Eleanor, J. & Carrea, L. (2020) Impact of the 2018 European heatwave on lake surface water temperature. *Inland Waters*, 10, 322–332. Available from: <https://doi.org/10.1080/20442041.2020.1712180>
- Wu, S., Yang, H., Luo, P., Luo, C., Li, H., Liu, M. et al. (2021) The effects of the cooling efficiency of urban wetlands in an inland megacity: a case study of Chengdu, Southwest China. *Building and Environment*, 204, 108128.
- Xu, L., Liu, H., Du, Q. & Wang, L. (2016) Evaluation of the WRF-lake model over a highland freshwater lake in southwest China. *Journal of Geophysical Research: Atmospheres*, 121, 13989–14005. Available from: <https://doi.org/10.1002/2016JD025396>
- Yang, J., Hu, L. & Wang, C. (2019) Population dynamics modify urban residents' exposure to extreme temperatures across the United States. *Science Advances*, 5, eaay3452. Available from: <https://doi.org/10.1126/sciadv.aay3452>
- Yang, L., Yang, Y., Shen, Y., Yang, J., Zheng, G., Smith, J. et al. (2024) Urban development pattern's influence on extreme rainfall occurrences. *Nature Communications*, 15, 3997.
- Yiou, P., Cattiaux, J., Faranda, D., Kadyrov, N., Jézéquel, A., Naveau, P. et al. (2020) Analyses of the northern European summer heatwave of 2018. *Bulletin of the American Meteorological Society*, 101(1), S35–S40.
- Yujie, R., Tang, X., Fan, T. & Kang, D. (2023) Does the spatial pattern of urban blue-green space at city-level affects its cooling efficiency? evidence from Yangtze River Economic Belt, China. *Landscape and Ecological Engineering*, 19, 363–379. Available from: <https://doi.org/10.1007/s11355-023-00540-2>
- Zhang, L., Meng, Q., Yao, S., Qian, J., Gao, J. & Wu, J. (2025) How to optimize urban blue space to maximize its cooling benefits? a case study in megacity of Beijing. *Building and Environment*, 270, 112502.
- Zhang, W., Yang, J., Yang, L. & Niyogi, D. (2022) Impacts of city shape on rainfall in inland and coastal environments. *Earth's Future*, 10, e2022EF002654. Available from: <https://doi.org/10.1029/2022EF002654>
- Zhu, D., Zhou, X. & Cheng, W. (2022) Water effects on urban heat islands in summer using WRF-UCM with gridded urban canopy parameters—a case study of Wuhan. *Building and Environment*, 225, 109528.
- Zhu, X., Li, D., Zhou, W., Ni, G., Cong, Z. & Sun, T. (2017) An idealized LES study of urban modification of moist convection. *Quarterly Journal of the Royal Meteorological Society*, 143, 3228–3243. Available from: <https://doi.org/10.1002/qj.3176>

SUPPORTING INFORMATION

Additional supporting information can be found online in the Supporting Information section at the end of this article.

How to cite this article: Chen, X., Gadde, S., Droste, A., Steeneveld, G.-J., Coenders-Gerrits, M. & Uijlenhoet, R. (2026) Assessing the role of urban blue space in summer outdoor thermal regulation in northwestern Europe: A hectometric Weather Research and Forecasting modelling on idealized urban landscape. *Quarterly Journal of the Royal Meteorological Society*, e70128. Available from: <https://doi.org/10.1002/qj.70128>